J. Fluid Mech. (2004), *vol.* 518, *pp.* 61–93.
DOI: 10.1017/S0022112004000771 Printed in the United Kingdom

Dynamic simulation of sphere motion in a vertical tube

By ZHAOSHENG YU[1], NHAN PHAN-THIEN[2] AND ROGER I. TANNER[1]

[1]School of Aerospace, Mechanical & Mechatronic Engineering, The University of Sydney, NSW 2006, Australia

[2]Division of Bioengineering, The National University of Singapore, Singapore 117576

(Received 20 December 2002 and in revised form 10 June 2004)

In this paper, the sedimentation of a sphere and its radial migration in a Poiseuille flow in a vertical tube filled with a Newtonian fluid are simulated with a finite-difference-based distributed Lagrange multiplier (DLM) method. The flow features, the settling velocities, the trajectories and the angular velocities of the spheres sedimenting in a tube at different Reynolds numbers are presented. The results show that at relatively low Reynolds numbers, the sphere approaches the tube axis monotonically, whereas in a high-Reynolds-number regime where shedding of vortices takes place, the sphere takes up a spiral trajectory that is closer to the tube wall than the tube axis. The rotation motion and the lateral motion of the sphere are highly correlated through the Magnus effect, which is verified to be an important (but not the only) driving force for the lateral migration of the sphere at relatively high Reynolds numbers. The standard vortex structures in the wake of a sphere, for Reynolds number higher than 400, are composed of a loop mainly located in a plane perpendicular to the streamwise direction and two streamwise vortex pairs. When moving downstream, the legs of the hairpin vortex retract and at the same time a streamwise vortex pair with rotation opposite to that of the legs forms between the loops. For Reynolds number around 400, the wake structures shed during the impact of the sphere on the wall typically form into streamwise vortex structures or else into hairpin vortices when the sphere spirals down. The radial, angular and axial velocities of both neutrally buoyant and non-neutrally buoyant spheres in a circular Poiseuille flow are reported. The results are in remarkably good agreement with the available experimental data. It is shown that suppresion of the sphere rotation produces significant large additional lift forces pointing towards the tube axis on the spheres in the neutrally buoyant and more-dense-downflow cases, whereas it has a negligible effect on the migration of the more dense sphere in upflow.

1. Introduction

Dynamic simulation of the motion of particles in a suspension is capable of providing both microscopic and macroscopic information on the suspension and consequently has become an important investigative tool for multiphase flow problems. A variety of methods have been developed over last two decades such as Stokesian Dynamics simulation (e.g. Brady & Bossis 1988), boundary-fitted-mesh-based direct numerical methods including the boundary element method (e.g. Phan-Thien, Tran-Cong & Graham 1991), the finite element method (e.g. Hu 1996; Johnson & Tezduyar 1997), the lattice-Boltzmann method (e.g. Aidun, Lu & Ding 1998), and the distributed

Lagrange multiplier-based fictitious domain method (referred to as the DLM method below). The last three can deal with the fluid inertial effect through the solution of the flow fields with the Navier–Stokes or lattice-Boltzmann equation, and are often referred to as direct numerical simulation methods (Hu, Joseph & Crochet 1992; Joseph 2003).

The DLM method was developed and first applied to particulate flow problems by Glowinski *et al.* (1997), and its detailed description can be found in Glowinski *et al.* (1999), Glowinski *et al.* (2001), and Glowinski (2003). The key features of the DLM method include a combined weak formulation for the fluid–particle system in which the mutual forces cancel (an explicit calculation of the hydrodynamic forces and torques on particles is not required, a fixed mesh is used for the computation of the flow field inside as well as outside the particles), remeshing due to the motion of particles is not required, and an operator-splitting technique for time discretization, resulting in a highly efficient and robust algorithm. With the DLM method, Pan, Joseph & Glowinski (2001) numerically simulated the sedimentation of 6400 circular particles in a two-dimensional cavity in the Rayleigh–Taylor instability, and Pan *et al.* (2002) investigated the fluidization of a bed of 1024 spherical particles; the results were in good agreement with experiments. Singh, Hesla & Joseph (2003) developed a collision strategy for the DLM method in which a slight overlap between particles is allowed. Yu *et al.* (2002*a*) substituted the so-called '$Q_1 - P_0$' finite element method for the 'twice-coarser' pressure element based one and the accuracy in predicting the lateral motion of particles was significantly improved due to the former's symmetric property. The migration of a circular particle in a channel or a plane Poiseuille flow (Yu *et al.* 2002*a*) and many particles moving in a circular Couette device (Yu, Tanner & Phan-Thien 2002*b*) were correctly produced with the $Q_1 - P_0$ method. The price for the enhanced accuracy is a higher cost and presumably less stability.

In this article, we present a new scheme obtained by replacing the finite element method with the half-staggered finite difference method for solving the fluid-flow problem. Compared to the $Q_1 - P_0$ finite element method, the new scheme has the same level of accuracy but is more efficient and robust particularly in the case of high Reynolds numbers. We then use the new scheme to simulate the motion of a sphere through a vertical tube filled with a Newtonian fluid at moderate and high Reynolds numbers. Two problems are investigated: the sphere sedimentation and its radial migration in Poiseuille flow. We focus on the motion characteristics and the wake structures at different Reynolds numbers for the former, and the effects of the relevant parameters on the migration rate for the latter. The main drawback of the DLM method is its relatively poor temporal and spatial convergence rates due to the operator-splitting technique and the discontinuity of velocity gradient on the particle boundary, as demonstrated by Yu *et al.* (2002*a*). Further, homogeneous meshes are often adopted in the DLM method, irrespective of the number of particles. We will put emphasis on a comparison between our results and available experimental data in an attempt to verify the DLM method as a reliable method for the direct numerical simulation of particulate flows, in particular at moderate Reynolds numbers. Glowinski *et al.* (2001) and Yu *et al.* (2002*a*) have shown that the DLM method is capable of predicting the settling velocity of a particle with reasonable accuracy, whereas the present work shows for the first time that the DLM method can also predict the rotation and the lateral migration of a particle in a shear flow with reasonable accuracy.

Feng, Hu & Joseph (1994*a*) and Yu *et al.* (2002*a*) investigated the motion of a circular particle sedimenting in a vertical channel of width $4D$, D being the particle diameter. Both groups observed that the particle monotonically approached

the centreline in a Reynolds number range corresponding to the unseparated flow regime for the flow past a fixed cylinder. The particle approached the centreline with an overshoot in a Reynolds number range corresponding to the steady and symmetric wake regime. In addition, the results of Yu *et al.* (2002*a*) showed that the particle migrated towards the centreline with rocking motion and eventually oscillated around the centreline with a fixed amplitude when the vortices were shed alternately from the sides of the particle and formed into Kármán vortex street. Since the wake structure of a sphere is different from that of a cylinder, one may wonder what kind of trajectory a sphere sedimenting in a tube at different Reynolds numbers will follow. The theory and experiments of Vasseur & Cox (1977) showed that a sphere settling in a vertical channel monotonically migrated towards the centreplane at a low (but not zero) Reynolds number. Previously reported works on dynamic simulation of the sedimentation of spheres in a vertical tube include Pan (1999) and Johnson & Tezduyar (1996, 1997); however, the analysis of a single sphere sedimenting at different Reynolds numbers has not been attempted. In the present paper, we will present the flow features, the settling velocities, the trajectories and the angular velocities of spheres sedimenting in a tube at different Reynolds numbers.

Particle migration in a Poiseuille flow is another important subject that has attracted much interest since Segré & Silberberg (1961, 1962) observed that a neutrally buoyant sphere migrated to a stable equilibrium position about 0.6 tube radius from the axis. The Segré–Silberberg effect was subsequently confirmed and investigated by others (e.g. Oliver 1962; Jeffrey & Pearson 1965; Karnis, Goldsmith & Mason 1966). When a particle is not neutrally buoyant, it was found that a *lagging* particle (e.g. a heavier particle in an upward moving fluid) migrates towards the tube axis, while a *leading* particle (e.g. a lighter particle in an upward moving fluid) migrates towards the tube wall (e.g. Jeffrey & Pearson 1965; Karnis *et al.* 1966; Denson, Christiansen & Salt 1966). The perturbation method has been widely employed to examine the inertia-induced lift force responsible for particle migration in a shear flow (e.g. Rubinow & Keller 1961; Saffman 1965; Cox & Brenner 1968; Ho & Leal 1974; Vasseur & Cox 1976; Schonberg & Hinch 1989; McLaughlin 1993; Hogg 1994; Asmolov 1999), and these works have successfully predicted the two-way migration in the neutrally buoyant case and the one-way migration in the non-neutrally buoyant case. Brenner (1966), Cox & Mason (1971) and Leal (1980) presented comprehensive reviews of experimental and theoretical works on particle migration. Dandy & Dwyer (1990), Cherukat, McLaughlin & Dandy (1999), and Kurose & Komori (1999) calculated numerically the lift force on a sphere fixed or rotating in a linear shear flow for a wide range of Reynolds numbers. To investigate the lateral migration of a freely moving particle, however, one has to resort to the dynamic simulation methods. Some studies on dynamical simulation of particle migration in a plane Poiseuille flow have been reported (e.g. Nott & Brady 1994; Feng, Hu & Joseph 1994*b*; Huang *et al.* 1997; Choi & Joseph 2001; Patankar *et al.* 2001*b*; Joseph & Ocando 2001); in the present work, we attempt to systematically examine the radial migration of a sphere in a circular Poiseuille flow for the first time.

The arrangement of the paper is as follows. In § 2, the new computational scheme is described and a dimensional analysis of the flow parameters is carried out for the sedimentation and Poiseuille flow cases. In § 3, we first present the results for the sedimentation of a sphere at different Reynolds numbers, and the structure of the hairpin vortex is discussed. Then the radial velocity, the angular velocity and the axial velocity of a sphere in Poiseuille flow are presented for both neutrally buoyant and non-neutrally buoyant cases. Conclusions are given in § 4.

2. Numerical model

Consider a particle with density ρ_d moving in a Newtonian fluid of density ρ_f and viscosity η. By introducing the scales L_c for length, U_c for velocity, L_c/U_c for time, $\rho_f U_c^2$ for pressure and $\rho_f U_c^2/L_c$ for distributed Lagrange multiplier, $\rho_d L_c^3$ for mass and $\rho_d L_c^5$ for moment of inertia, the dimensionless weak formulation of the governing equations in the case of Dirichlet boundary conditions is stated as follows:

For $t > 0$, find $u \in W_{u\Gamma}$, $p \in L_0^2(\Omega)$, $\lambda \in \Lambda(t)$, $U \in R^3$, and $\Omega \in R^3$ satisfying

(*a*) *the combined momentum equation*

$$\begin{aligned}\int_\Omega \left(\frac{\partial \boldsymbol{u}}{\partial t} + \boldsymbol{u}\cdot\nabla\boldsymbol{u}\right)\cdot\boldsymbol{v}\,d\boldsymbol{x} - \int_\Omega p\nabla\cdot\boldsymbol{v}\,d\boldsymbol{x} + \frac{1}{Re}\int_\Omega (\nabla\boldsymbol{u})^T : \nabla\boldsymbol{v}\,d\boldsymbol{x} \\ + (\rho_r - 1)\left[M\left(\frac{d\boldsymbol{U}}{dt} - Fr\frac{\boldsymbol{g}}{g}\right)\cdot\boldsymbol{V} + J\frac{d\Omega}{dt}\cdot\boldsymbol{\xi}\right] - \boldsymbol{F}'\cdot\boldsymbol{V} \\ = \langle\boldsymbol{\lambda}, \boldsymbol{v} - (\boldsymbol{V} + \boldsymbol{\xi}\times\boldsymbol{r})\rangle_{P(t)}, \quad \text{for all } \boldsymbol{v}\in W_0(t),\ \boldsymbol{V}\in R^3,\ \boldsymbol{\xi}\in R^3;\end{aligned} \tag{2.1}$$

(*b*) *the incompressibility constraint*

$$\int_\Omega q\nabla\cdot\boldsymbol{u}\,d\boldsymbol{x} = 0, \quad \text{for all } q\in L^2(\Omega); \tag{2.2}$$

(*c*) *and the rigid-body motion constraint*

$$\langle\boldsymbol{\mu}, \boldsymbol{u} - (\boldsymbol{U} + \Omega\times\boldsymbol{r})\rangle_{P(t)} = 0, \quad \text{for all } \boldsymbol{\mu}\in\Lambda(t). \tag{2.3}$$

Here, $\boldsymbol{u}$, p, $\boldsymbol{U}$, Ω and λ are the fluid velocity, the pressure, the particle translational and angular velocities, and the distributed Lagrange multiplier, respectively, and $\boldsymbol{v}, q, \boldsymbol{V}, \boldsymbol{\xi}$ and $\boldsymbol{\mu}$ are their corresponding variances. M and J are the mass and the moment of inertia of the particle, respectively. Here, $\boldsymbol{r}$ is the position vector with respect to the centre of the particle, $\boldsymbol{F}'$ is the repelling force from the neighbouring particles (if required) or from the solid wall preventing the particle from penetrating other particles or the wall, and $\boldsymbol{g}$ is the acceleration due to gravity. There are three parameters: particle to fluid density ratio $\rho_r = \rho_d/\rho_f$, the Reynolds number $Re = \rho_f U_c L_c/\eta$ and the Froude number $Fr = gL_c/U_c^2$. Here the Froude number represents the relative importance of gravity and inertia.

The following solution or variance spaces are used:

$$\left.\begin{aligned} W_{u\Gamma} &= \{\boldsymbol{v}\in H^1(\Omega)^3 \mid \boldsymbol{v} = \boldsymbol{u}_\Gamma(t) \text{ on } \Gamma\},\\ W_0 &= \{\boldsymbol{v}\in H^1(\Omega)^3 \mid \boldsymbol{v} = 0 \text{ on } \Gamma\},\\ L_0^2 &= \left\{q\in L^2(\Omega)\,\middle|\,\int_\Omega q\,d\boldsymbol{x} = 0\right\},\end{aligned}\right\} \tag{2.4}$$

and $\Lambda(t)$ is an appropriate space by which the constraint of rigid-body motion in $P(t)$ is enforced; $\langle,\rangle$ is an inner product defined in $\Lambda(t)$. $P(t)$ signifies the region inside and including the particle boundary, Ω the entire computational domain including both the interior and exterior of the particle, and Γ the boundary of Ω.

Although the formulations above involve only one particle and Newtonian fluids, the extension to the many-particle case or the viscoelasticity case is straightforward.

2.1. *Computational scheme*

The operator-splitting technique was proposed by Glowinski *et al.* (1999) to decompose the system (2.1)–(2.3) into sub-systems. The essential step is to divide the original

fluid/solid system into a fluid-flow part and a particle-motion part in the following forms:

(*a*) Fluid-flow part: find $\boldsymbol{u}^{\#} \in W_{\boldsymbol{u}\Gamma}$, $p \in L_0^2(\Omega)$, satisfying

$$\int_\Omega \left(\frac{\boldsymbol{u}^{\#} - \boldsymbol{u}^n}{\Delta t} + \boldsymbol{u} \cdot \nabla \boldsymbol{u} \right) \cdot \boldsymbol{v} \, \mathrm{d}\boldsymbol{x} - \int_\Omega p \nabla \cdot \boldsymbol{v} \, \mathrm{d}\boldsymbol{x} + \frac{1}{Re} \int_\Omega (\nabla \boldsymbol{u})^T : \nabla \boldsymbol{v} \, \mathrm{d}\boldsymbol{x} = 0, \quad \text{for all } \boldsymbol{v} \in W_0(t), \tag{2.5}$$

$$\int_\Omega q \nabla \cdot \boldsymbol{u}^{\#} \, \mathrm{d}\boldsymbol{x} = 0, \quad \text{for all } q \in L_h^2. \tag{2.6}$$

(*b*) Particle-motion part: find $\boldsymbol{u}^{n+1} \in W_{\boldsymbol{u}\Gamma}$, $\boldsymbol{\lambda} \in \Lambda(t)$, $\boldsymbol{U}^{n+1} \in R^3$, and $\boldsymbol{\Omega}^{n+1} \in R^3$ satisfying

$$\int_\Omega \left(\frac{\boldsymbol{u}^{n+1} - \boldsymbol{u}^{\#}}{\Delta t} \right) \cdot \boldsymbol{v} \, \mathrm{d}\boldsymbol{x} + (\rho_r - 1) \left[M \left(\frac{\boldsymbol{U}^{n+1} - \boldsymbol{U}^n}{\Delta t} - Fr \frac{\boldsymbol{g}}{g} \right) \cdot \boldsymbol{V} + J \frac{\boldsymbol{\Omega}^{n+1} - \boldsymbol{\Omega}^n}{\Delta t} \cdot \boldsymbol{\xi} \right] - \boldsymbol{F}' \cdot \boldsymbol{V} = \langle \boldsymbol{\lambda}, \boldsymbol{v} - (\boldsymbol{V} + \boldsymbol{\xi} \times \boldsymbol{r}) \rangle_{P(t)}, \quad \text{for all } \boldsymbol{v} \in W_0(t), \boldsymbol{V} \in R^3, \boldsymbol{\xi} \in R^3, \tag{2.7}$$

$$\langle \boldsymbol{\mu}, \boldsymbol{u}^{n+1} - (\boldsymbol{U}^{n+1} + \boldsymbol{\Omega}^{n+1} \times \boldsymbol{r}) \rangle_{P(t)} = 0, \quad \text{for all } \boldsymbol{\mu} \in \Lambda(t). \tag{2.8}$$

This splitting results in substantial simplification of the algorithm and improvement in the efficiency and robustness. On the other hand, it is a significant source of computational errors. Particularly in the case of low Reynolds numbers where viscous diffusion dominates the flow, a very small time step is needed for acceptable accuracy (Yu *et al.* 2002*a*). Our recent numerical experiments show that this difficulty can be alleviated by keeping the multiplier term at the previous time step in the fluid-flow problem (2.5) and replacing the Lagrange-multiplier with the multiplier difference in the particle-motion problem (2.7).

Equations (2.5)–(2.6) represent the weak formulation of the Navier–Stokes and continuity equations

$$\left. \begin{aligned} &\frac{\partial \boldsymbol{u}}{\partial t} + \boldsymbol{u} \cdot \nabla \boldsymbol{u} = -\nabla p + \frac{1}{Re} \nabla^2 \boldsymbol{u}, \\ &\nabla \cdot \boldsymbol{u} = \boldsymbol{0}. \end{aligned} \right\} \tag{2.9}$$

We suggest solving equations (2.9) using a finite difference scheme as an approximation solution to the fluid-flow problem, instead of solving equations (2.5)–(2.6) directly with the finite element method. Generally speaking, the finite difference method is better suited to problems posed in a regular domain than the finite element method. The widely used projection method is employed here, which is stated as follows:

$$\left. \begin{aligned} &\frac{\boldsymbol{u}^* - \boldsymbol{u}^n}{\Delta t} + (\boldsymbol{u} \cdot \nabla \boldsymbol{u})^n = \frac{1}{Re} \nabla^2 \boldsymbol{u}^*, \\ &\boldsymbol{u}^* = \boldsymbol{u}_\Gamma \text{ on } \Gamma; \end{aligned} \right\} \tag{2.10}$$

$$\left. \begin{aligned} &\nabla^2 p = \frac{\nabla \cdot \boldsymbol{u}^*}{\Delta t}, \\ &\frac{\partial p}{\partial n} = 0 \text{ on } \Gamma; \end{aligned} \right\} \tag{2.11}$$

$$\frac{\boldsymbol{u}^{\#} - \boldsymbol{u}^*}{\Delta t} = -\nabla p. \tag{2.12}$$

Equation (2.10) is an advection–diffusion problem and can be further decomposed into three diagonal systems with the ADI technique. We adopt the following version:

$$\left.\begin{aligned}
&\frac{\boldsymbol{u}^{k+1/3}-\boldsymbol{u}^{k}}{\Delta t/3}+(\boldsymbol{u}\cdot\nabla u)^{k}=\frac{1}{Re}\left(\nabla_x^2\boldsymbol{u}^{k+1/3}+\nabla_y^2\boldsymbol{u}^{k}+\nabla_z^2\boldsymbol{u}^{k}\right),\\
&\frac{\boldsymbol{u}^{k+2/3}-\boldsymbol{u}^{k+1/3}}{\Delta t/3}+(\boldsymbol{u}\cdot\nabla u)^{k+1/3}=\frac{1}{Re}\left(\nabla_x^2\boldsymbol{u}^{k+1/3}+\nabla_y^2\boldsymbol{u}^{k+2/3}+\nabla_z^2\boldsymbol{u}^{k+1/3}\right),\\
&\frac{\boldsymbol{u}^{k+1}-\boldsymbol{u}^{k+2/3}}{\Delta t/3}+(\boldsymbol{u}\cdot\nabla u)^{k+2/3}=\frac{1}{Re}\left(\nabla_x^2\boldsymbol{u}^{k+2/3}+\nabla_y^2\boldsymbol{u}^{k+2/3}+\nabla_z^2\boldsymbol{u}^{k+1}\right),
\end{aligned}\right\} \tag{2.13}$$

in which we set $\boldsymbol{u}^k=\boldsymbol{u}^n$ and $\boldsymbol{u}^*=\boldsymbol{u}^{k+1}$.

A half-staggered finite difference scheme is employed to discretize equations (2.10)–(2.12) in space where the nodes of all velocity components are co-located and the pressure nodes are staggered with the velocity nodes. All derivative terms are discretized with the central difference scheme. The resulting spatial scheme is exactly the same as obtained from the Q_1-P_0 finite element method used by Yu *et al.* (2002*a*) where the trapezoidal rule is employed for the elemental integration. However, the finite element method involves Uzawa iteration at every time step and the computational cost per iteration is comparable to that per time step for the current method. Hence, it is clear that the current method is much more efficient, and furthermore we found it more robust for solving high-Reynolds-number flows, while the two methods were observed to produce almost same results. A completely staggered mesh is usually used in association with the projection method, and the incorporation of it into the DLM method is a subject of further study.

Equation (2.11) is an elliptic problem with a homogeneous Neumann boundary condition and can be efficiently solved by using a combination of FFT and a tri-diagonal system solver (Yu *et al.* 2002*a*).

The reader is referred to Glowinski *et al.* (1999, 2001), Pan & Glowinski (2002) and Yu *et al.* (2002*a*) for the numerical method to solve the particle-motion problem (2.7)–(2.8). In particular, Pan & Glowinski (2002) solved the difficulty arising from the singularity of the neutrally buoyant case in the DLM formulation (2.1), which however does not exist in another version of the DLM formulation (Patankar *et al.* 2000). An analytical solution to equations (2.7)–(2.8) was derived by Glowinski *et al.* (2001) with an approximation that the velocity field outside the particle boundary remains unchanged for this sub-problem, and the difficulty in the neutrally buoyant case is also circumvented. However, they reported that the solution obtained with the collocation point method is of better quality. In this study the collocation point (CP) method is used for the sedimentation case and the collocation element (CE) method for the Poiseuille flow. The CE method was proposed by Yu *et al.* (2002*a*) and was found to give a smoother solution (but not necessarily more accurate) than that obtained with the CP method. The control points for the CP method are located in a sequence of parallel planes that are evenly distributed inside the sphere and their distribution in each plane has the same pattern as reported by Yu *et al.* (2002*a*). For the CE method, we generate evenly distributed points in a cube covering the sphere, leave out those outside the sphere, and enforce the constraint of rigid-body motion using the weighted-average values of the velocities at each remaining point and its surrounding six points aligned with the axis directions. The mesh sizes (distance between neighbouring control points) for both the CE and CP methods are slightly coarser than the velocity mesh size. Another set of Lagrange multipliers is introduced

to impose the boundary condition at the tube wall with the CE method, as the computation of flow fields is performed in a quadrant.

2.2. *Analysis of dimensionless governing parameters*

2.2.1. *Sedimentation case*

Now consider the problem of a sphere sedimenting in an infinitely long vertical tube filled with a Newtonian fluid. Once the initial conditions of the fluid and the particle are given, the flow is uniquely determined by the parameters (ρ_f, ρ_d, η, g, a, R), which denote the fluid density, the particle density, the fluid viscosity, the gravitational acceleration, the radius of the sphere and the radius of the tube, respectively. There are six dimensional parameters, thus, three dimensionless parameters are required, which can be (ρ_r, Re, λ_a), where $\lambda_a = a/R$. Following the ideas of Yu *et al.* (2002*a*), let the diameter of the sphere $2a$ be the characteristic length L_c and choose the characteristic velocity U_c close to the terminal setting velocity by reasonably combining the dimensional parameters. For the case of strong inertial effect, we define U_c by

$$U_c = \sqrt{\frac{8a}{3}|\rho_r - 1|g} \tag{2.14}$$

so that

$$C_D = \frac{\frac{4}{3}\pi a^3|\rho_d - \rho_f|g}{\frac{1}{2}\pi a^2 \rho_f U_T^2} = \frac{U_c^2}{U_T^2} = \frac{1}{(U_T^*)^2}, \tag{2.15}$$

and

$$N_D = \frac{4\rho_f^2|\rho_d - \rho_f|g(2a)^3}{3\eta^2} = Re^2, \tag{2.16}$$

where U_T and U_T^* are the dimensional and dimensionless terminal sedimenting velocity, respectively, C_D is the drag coefficient, and N_D is sometimes called the 'Best number' (Clift, Grace & Weber 1978). The terminal velocity can be more conveniently obtained from the relationship between Re_T and N_D than between C_D and Re_T since N_D is independent of the terminal velocity, whereas the other two are not. The Froude number becomes

$$Fr = \frac{3}{4|\rho_r - 1|}. \tag{2.17}$$

The Reynolds number Re_T , which is based on the terminal settling velocity, can be calculated from

$$Re_T = U_T^* Re. \tag{2.18}$$

In this study, Re_T is also used to represent the Reynolds number based on the mainstream velocity in experiments or static simulations.

2.2.2. *Poiseuille flow case*

For the case of spherical particles moving in a Poiseuille flow, we add the initial maximum velocity at the centreline U_m into the parameter group and an additional dimensionless parameter λ_f is accordingly defined by

$$\lambda_f = \frac{U_f}{U_m}, \tag{2.19}$$

where U_f is the Stokes free-fall velocity of a sphere, i.e.

$$U_f = 4a^2|\rho_d - \rho_f|g/18\eta. \tag{2.20}$$

U_m and R are taken as the characteristic velocity and length, respectively. The corresponding Reynolds number is the so-called tube Reynolds number and we denote it by Re_t. The Froude number has the form

$$Fr = \frac{9\lambda_f}{2|\rho_r - 1|\lambda_a^2 Re_t}. \tag{2.21}$$

Some other commonly used Reynolds numbers can be expressed in terms of Re_t, λ_a and λ_f, such as

$$\text{shear Reynolds number } Re_s = \frac{\rho_f U_m (2a)^2}{R\eta} = 4\lambda_a^2 Re_t, \tag{2.22}$$

$$\text{free-fall Reynolds number } Re_f = \frac{\rho_f U_f a}{\eta} = \lambda_a \lambda_f Re_t, \tag{2.23}$$

$$\text{slip Reynolds number } Re_{slip} = \frac{\rho_f |\boldsymbol{U}_s|(2a)}{\eta} = 2\frac{|\boldsymbol{U}_s|}{U_m}\lambda_a Re_t. \tag{2.24}$$

In equation (2.24), the slip velocity $\boldsymbol{U}_s$ was found to have the following form in a Poiseuille flow (Brenner 1966)

$$\boldsymbol{U}_s = \left\{ \pm U_f \left[1 - f(r)\frac{a}{R} \right] - \frac{2}{3}\left(\frac{a}{R}\right)^2 U_m \right\} \boldsymbol{e}_z \tag{2.25}$$

where $f(r)$ denotes a function of radial position and $\boldsymbol{e}_z$ is the flow direction. The choice of the positive or negative sign for the first term on the right-hand side of (2.25) depends on whether the sphere leads or lags the fluid, In addition, one can find the following relationships for the sedimentation case and the Poiseuille flow case:

$$\left.\begin{aligned} Re &= 4\sqrt{3Re_f}, \\ \frac{U_T}{U_m} &= 2\sqrt{3}U_T^* \frac{\lambda_f}{\sqrt{Re_f}}. \end{aligned}\right\} \tag{2.26}$$

In equation (2.26), U_T^* can be obtained from the figure plotting Re_T versus $N_D^{1/3}$ given by Clift *et al.* (1978). The above equations are useful to estimate the real dimensionless slip velocity of the sphere in Poiseuille flow subjected to the effects of the wall and inertia.

Apart from the parameter group (Re_t, λ_a, λ_f, ρ_r), the pressure gradient is needed for uniquely determining the motion of the particles in the case of pressure-driven flows. Two approaches to deal with the pressure gradient can be considered: one is to keep the pressure gradient unchanged with time, as employed by Choi & Joseph (2001) and Huang & Joseph (2000), and the other is to keep the flow flux invariant, from which the pressure gradient can be determined. The choice should agree with the experimental conditions to be compared. Note that there are five dimensionless control parameters including the pressure gradient for the former and four for the latter (U_m is usually taken as twice the mean velocity if the velocity profile deviates from a parabolic distribution). Nevertheless, if one is only interested in the results at the steady state (if exists) and defines Re_t and λ_f by using the steady flow flux, then the constant pressure gradient given for the latter can be excluded from the control parameter group since the relationship between the pressure gradient and the flow flux at the steady state is unique.

Maintaining the pressure gradient invariant is the approach used in this study for simplicity, and the pressure gradient is set to be $(-4/Re_t)$, the value required for

just sustaining the steady circular Poiseuille flow of Newtonian fluids. Only a single neutrally buoyant or slightly denser particle is involved here and its effect on the flow flux is small; therefore, the tube Reynolds number is expected to change only slightly during the simulations and we will adopt the initial tube Reynolds number for analysing flows.

For a sphere, the dimensionless mass M and moment of inertia J are $\frac{4}{3}\pi(a^*)^3$ and $\frac{2}{5}(a^*)^2M$, respectively. Here, a^* represents the dimensionless sphere radius, being $1/2$ for the sedimentation case and λ_a for the Poiseuille flow case.

For both problems studied here, the sphere will travel a long distance along the streamwise direction. In order to save computational costs, we introduce a periodic boundary condition for the Poiseuille flow case and the periods used range from $8D$ to $11D$, D being the sphere diameter. For the sedimentation case, we let the computational domain move with the sphere, and the method is simply this: once the sphere falls below than a designated position z', the computational domain is moved downwards one mesh distance so that the streamwise motion of the sphere in the frame of the computational domain is largely restricted within a mesh above z'. For simplicity, the velocities on the downstream boundary are kept unchanged till the next update of the computation domain. This method was also used by Yu *et al.* (2002*a*) to simulate the sedimentation of a circular particle in a vertical channel. The computational tube lengths range from $15D$ to $25D$, for varying Reynolds numbers, and the designated position is located $4D$ from the upstream boundary.

Throughout this study, the time step is set to be 0.01 and one sphere diameter covers 11.52–16 spatial meshes for various cases. The results of a convergence test for the Poiseuille flow case will be presented.

3. Results and discussion

3.1. *Sedimentation of a sphere*

A Cartesian coordinate system shown in figure 1(*a*) is used for computation and description of the motion of spheres. Gravity is directed along the negative z-axis.

3.1.1. *Motion behaviours at different Reynolds numbers*

We now analyse the motion of spheres falling in a tube of $\lambda_a = 0.2$ at $Re = 20$, 100, 200, 300 and 400, respectively. For each case, the sphere is released from $(x_0, y_0) = (-1.25, 0)$ and ρ_r is set to 1.5. The role of ρ_r will be discussed in the Poiseuille flow case. The flow field, settling velocities, trajectories and angular velocities of the spheres are shown in figures 1–4, respectively.

Numerous experiments and computations (e.g. Magarvey & Bishop 1961; Natarajan & Acrivos 1993; Johnson & Patel 1999; Tomboulides & Orszag 2000) showed that there are four flow regimes for the flow past a sphere at moderate Reynolds numbers: unseparated flow ($Re_T < 20$), a steady and axisymmetric wake ($20 < Re_T < 210$), a non-axisymmetric wake ($210 < Re_T < 270$) and shedding of vortices ($Re_T > 270$). As can be seen from figure 3(*a*), steady terminal settling velocities at $Re = 200$ and higher cannot be obtained from our simulations, thus, more conveniently, we take a settling Reynolds number Re_{max} that is based on the maximum velocity observed during the simulation as a characteristic Reynolds number for each case. The values of Re_{max} are 7.94, 83.8, 197, 306 and 424, corresponding to $Re = 20$, 100, 200, 300 and 400, respectively. Therefore, $Re = 20$ corresponds to Regime A, 100 and 200 to Regime B, and 300 and 400 to Regime D, respectively.

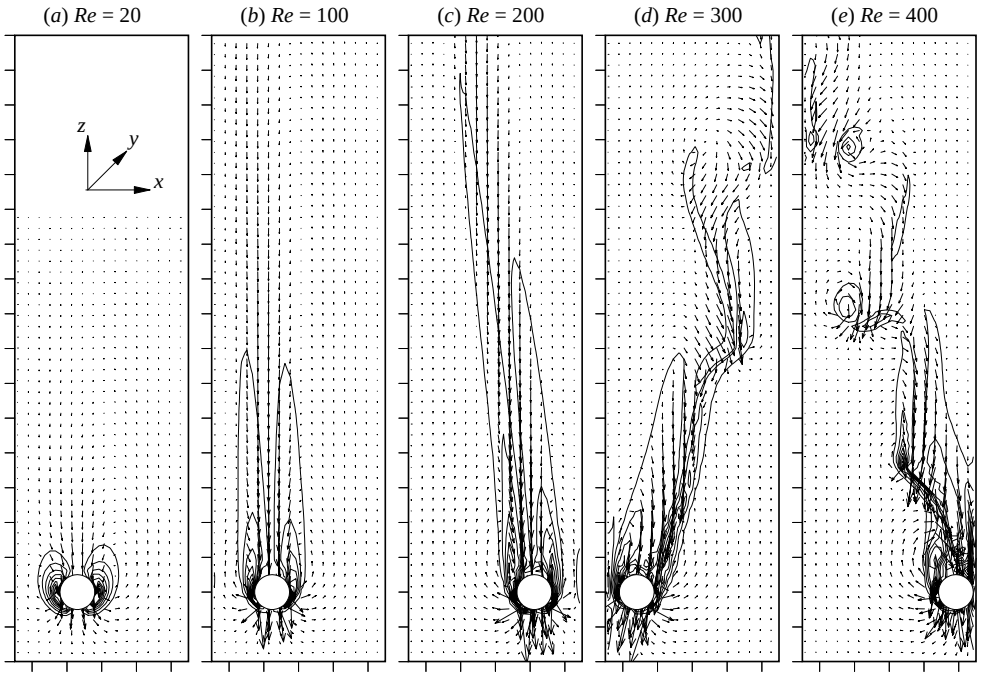

FIGURE 1. Contours of ω_y and velocity fields at different Reynolds numbers in the (x, z) planes. (*a*) $t = 30$; (*b*) $t = 30$; (*c*) $t = 40$; (*d*) $t = 50$ and (*e*) $t = 30$. $\lambda_a = 0.2$; $(x_0, y_0) = (-1.25, 0)$.

Typical flow features for the sedimentation of the spheres at different Reynolds numbers are presented in figure 1. In the cases of $Re = 20$ and $Re = 100$, non-axisymmetric vortex structures are observed when the spheres migrate towards the tube axis, and they become axisymmetric when the spheres reach the tube axis. At $Re = 200$, the circulation zone behind the sphere is very long and the wake is highly non-axisymmetric. Consistent with experimental observations of Achenbach (1974), as Re increases up to 400, the vortex sheets behind the sphere roll up strongly due to the Kelvin–Helmholtz instability, and are shed, forming hairpin vortices. At $Re = 300$, shedding of vortices can be observed, but the strong rollup of vortex sheets never takes place and the vortex structures in the wake are not organized as regularly as at $Re = 400$. Shedding of vortices without rollup was also reported by Johnson & Patel (1999) for the flow past a fixed sphere at $Re_T = 300$.

Figure 2 shows that the sphere at both $Re = 20$ and 100 monotonically approaches the tube axis and takes the tube axis as its equilibrium position. The sphere at $Re = 200$ moves pass the tube axis until reaching a position about halfway between the tube wall and the tube axis. It then moves back and oscillates around the tube axis from the (x, z)-plane view during our simulation time. The motion of the sphere in the (x, z)-plane is unstable and the sphere is observed to move out of this plane. The subsequent trajectory of the sphere may be taken in a qualitative sense only, since the departure of the sphere from the symmetric plane is caused by randomly generated numerical disturbances and even the deviation direction is not controlled. For convenience, we refer to the stage when the sphere moves in the (x, z)-plane as Stage One and the subsequent stage out of the (x, z)-plane as Stage Two. The sphere behaviour at $Re = 300$ is similar to that at $Re = 200$ and the main difference is that for the former the sphere can approach the wall much closer. From an (x, y)-plane view,

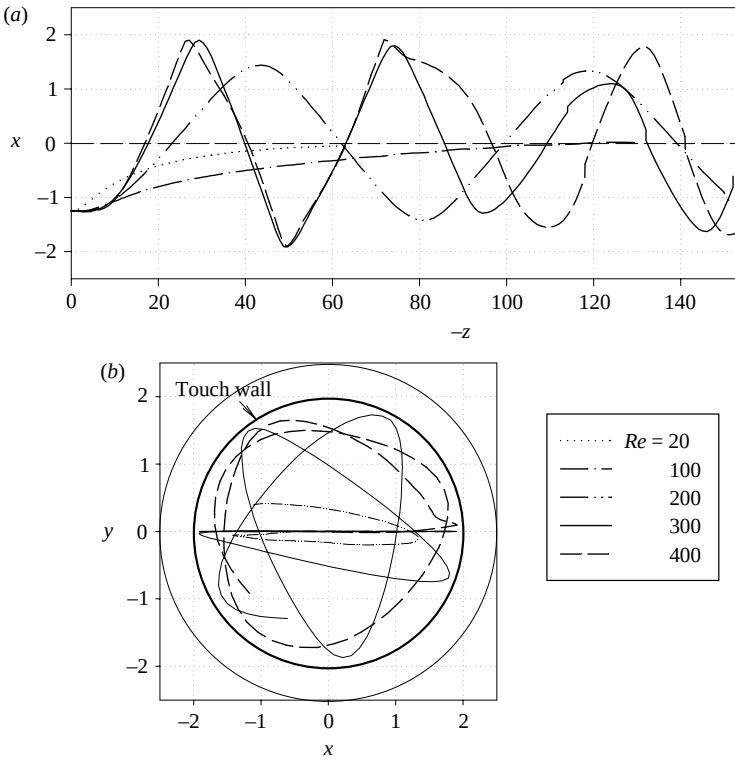

FIGURE 2. Trajectories of spheres at different Reynolds numbers: (*a*) (x, z)-plane view; (*b*) (x, y)-plane view. $\lambda_a = 0.2$; $(x_0, y_0) = (-1.25, 0)$.

the sphere at $Re = 300$ moves along a curve, not a straight line from one side to another at Stage Two, and it is interesting that the curvature increases rapidly when the sphere approaches close to the wall, unlike the case of elastic collision. The (x, y)-trajectory of the sphere at $Re = 400$ is almost parallel to the tube wall at Stage Two and we do not know whether it will eventually become concentric with the tube wall. The sphere at $Re = 300$ never touches the wall in our simulation. However, at $Re = 400$, our code fails to run when the sphere moves back into the (x, z)-plane and approaches the wall very closely, hence a repulsive force (Glowinski *et al.* 1999) is invoked when the distance between the sphere surface and the wall is smaller than the mesh size, which is the only case in this study where special treatment is required. We suspect that the hydrodynamic repulsive force, or lubrication force, is capable of preventing a collision between the sphere and the wall, and the dubious sudden jump in the rotation at time around 74 for the case of $Re = 400$ in figure 4 can be removed, provided the mesh is fine enough. However, we did not attempt to do this because we adopt a homogeneous mesh and the computational cost of enhancing the resolution would be prohibitively high. We are mainly interested the qualitative behaviour of the sphere there. In practice, it is not possible for any direct numerical simulation methods to produce an accurate lubrication force when two bodies approach very closely.

Figure 3(*a*) shows the time developments of the settling velocities at the different Reynolds numbers and figure 3(*b*) shows comparisons between Re_{max} and experimental Re_T obtained for spheres fixed on the tube axis (Clift *et al.* 1978). The settling velocity increases rapidly at initial times for all cases. Subsequently, for $Re = 20$, the

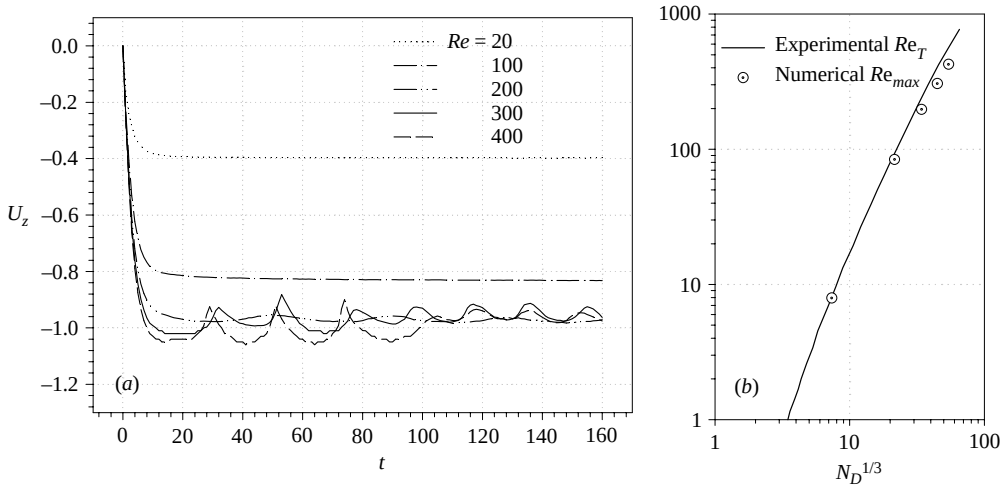

FIGURE 3. (*a*) Time development of settling velocities at different Reynolds numbers and (*b*) settling Reynolds numbers based on the maximum settling velocities observed during the simulations, with comparison to the experimentally obtained terminal settling Reynolds numbers for a sphere on the tube axis (Clift *et al.* 1978). $\lambda_a = 0.2; (x_0, y_0) = (-1.25, 0)$.

settling velocity basically remains unchanged during the sphere migration towards the tube axis and for $Re = 100$, the settling velocity increases very slightly. For the other cases, the settling velocity oscillates due to the effects of the wall. As a rule, the velocity increases as the sphere moves closer to the tube axis and decreases as the sphere moves closer to the wall. For $Re = 300$ and 400, the reduction in the magnitude of the velocity is significant when the sphere approaches the wall closely. Re_{max} for $Re = 20$ and 100 is basically equivalent to Re_T and a good agreement with the experimental data is found, as illustrated in figure 3(*b*). A pronounced disparity between Re_{max} and experimental Re_T is observed for $Re = 200$, 300 and 400, and the lateral and rotating motion of the sphere when it reaches the tube axis in the simulation is partly responsible for this disparity. Although Yu *et al.* (2002*a*) observed that, for the case of relatively high Reynolds number, the DLM method can predict roughly the same settling velocities of a circular particle as those obtained with the finite element method (Feng *et al.* 1994*a*), it appears to gives systematically smaller settling velocities of a sphere compared to the experiments. The reason is unclear; however, it is possible that the numerical error is increased as Re increases. If this is true, there are two remedies: one is to simply take a hydrodynamic radius (obtained from numerical results) rather than the physical radius as the computational size of the sphere, which is widely used in the lattice-Boltzmann method (e.g. Nguyen & Ladd 2002); and the other is to adopt more sophisticated spatial and time discretization schemes for higher accuracy.

It was observed that a circular particle settling a vertical channel rotates in an anomalous way, i.e. as if rolling up the nearby wall, when it migrates towards the channel centreline (Feng *et al.* 1994*a*; Yu *et al.* 2002*a*). Not surprisingly, the spheres behave in a similar way at $Re = 20$ and $Re = 100$. For $Re = 200$ or higher and at Stage One, the sphere retains its previous rotation direction while passing through the tube axis till it begins to move back to start the next cycle (figure 4). The difference between the case of $Re = 200$ and the case of $Re = 300$ or 400 is that the magnitude of the angular velocity for the latter keeps increasing until the sphere approaches the

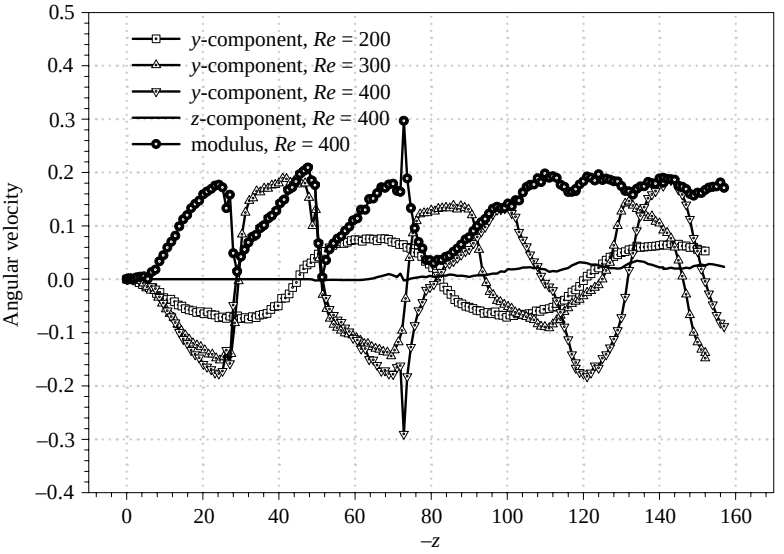

FIGURE 4. Angular velocities versus streamwise positions at $Re = 200$, 300 and 400. $\lambda_a = 0.2$; $(x_0, y_0) = (-1.25, 0)$.

wall closely and consequently it changes violently in the vicinity of the wall, whereas the angular velocity for the former changes much more smoothly at the times of cycle shift. With the spheres moving out of the (x, z)-plane, the other two components of the angular velocity become significant. The streamwise component $\boldsymbol{\Omega}_z$ and the modulus of the angular velocity $|\boldsymbol{\Omega}|$ for $Re = 400$ are depicted in figure 4 and we can see that at Stage Two $|\boldsymbol{\Omega}|$ does not change much with time and is almost one order of magnitudes greater than $\boldsymbol{\Omega}_z$. The sign of $\boldsymbol{\Omega}_z$ does not change with time; the sphere maintains the direction of its streamwise rotation while spiralling down in the tube.

It is interesting to find that the rotation motion and the lateral motion of the sphere are highly correlated through the Magnus effect. Based on the potential flow theory, the Magnus force on a moving and rotating body has the form

$$\boldsymbol{F} = \rho_f \boldsymbol{\Gamma} \times \boldsymbol{U} \tag{3.1}$$

in which $\boldsymbol{\Gamma}$ and $\boldsymbol{U}$ are the circulation and translational velocities of the body with respect to the fluid, respectively. In the current problem, we take $\boldsymbol{U}$ as the settling velocity directed downward. From the (x, y)-plane view, the angular velocity vector is always directed toward the right-hand side of the (x, y)-trajectory for each case and any time, as indicated in figure 4 and figure 2. Clearly, the resulting Magnus force has the same direction as the lateral motion of the sphere (figure 2). Therefore, the Magnus force appears to be a primary driving forces for the lateral motion of the sphere. Nevertheless, the theoretical analyses (Vasseur & Cox 1976, 1977) showed that the migration rate of a sphere is independent of its rotation at small λ_a and Re, indicating that in this case the Magnus effect is not relevant to the lateral motion of the sphere. In order to examine the effect of the Magnus force on the sphere migration at moderate λ_a and Re, we conducted simulations where rotation motion of the sphere is not allowed and compare the results to the free-rotation cases at the same Reynolds numbers in figure 5. We see that the suppression of the rotation does not eliminate the lateral migration of the spheres, but reduces the migration

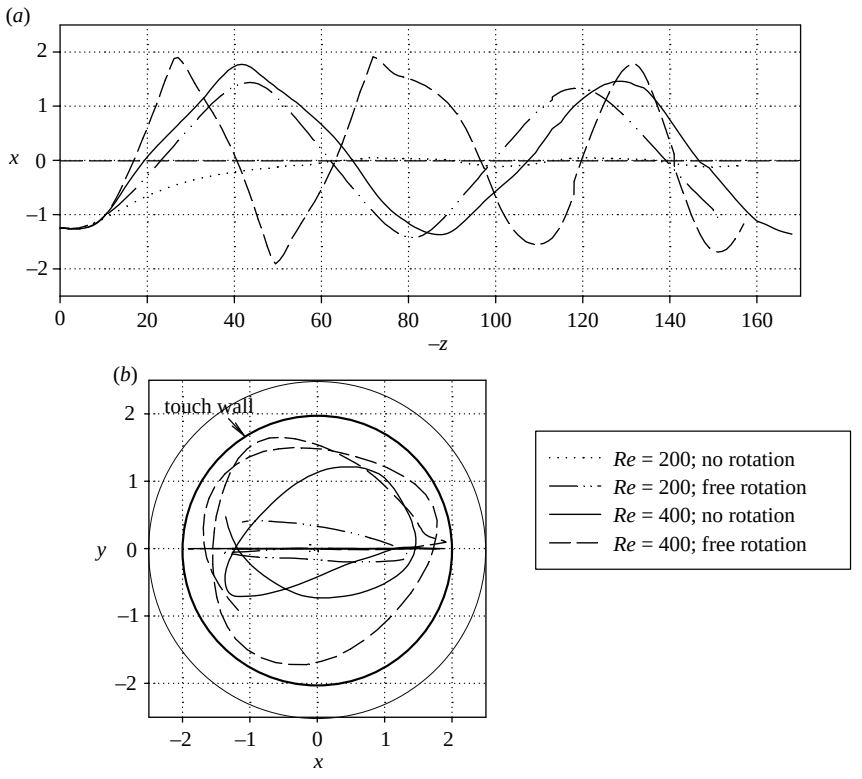

FIGURE 5. Comparison of the trajectories of spheres between the cases of free rotation and no rotation: (*a*) (x, z)-plane view; (*b*) (x, y)-plane view. $\lambda_a = 0.2$; $(x_0, y_0) = (-1.25, 0)$.

rate and the migration distance significantly for both $Re = 200$ and $Re = 400$. For the case of $Re = 200$, the sphere with no rotation approaches the tube axis monotonically and stays there, oscillating with a very small amplitude. Its terminal settling velocity is around unity, only slightly larger than that in the free-rotation case, indicating that the rotation and lateral motions of the sphere do not significantly affect the streamwise drag.

The main differences between a circular particle settling in channel (Yu *et al.* 2002*a*) and a sphere settling in a tube are:

(*a*) in the steady symmetric wake Re_T regime, the circular particle approaches the channel centreline with an overshoot, whereas the sphere may approach the tube axis monotonically;

(*b*) shedding of vortices from alternate sides of the circular particle gives rise to a rocking motion for the particle, whereas no obvious effects of vortex shedding on the motion of the sphere in a tube are observed;

(*c*) at high Re, the circular particle eventually oscillates around the channel centreline with a small and fixed amplitude, whereas the sphere takes up a spiral trajectory that is closer to the tube wall than the tube axis.

These differences are not surprising, since the motion of the fluids is restricted in a plane for the former, whereas the fluids can move around the sphere in a three-dimensional space for the latter.

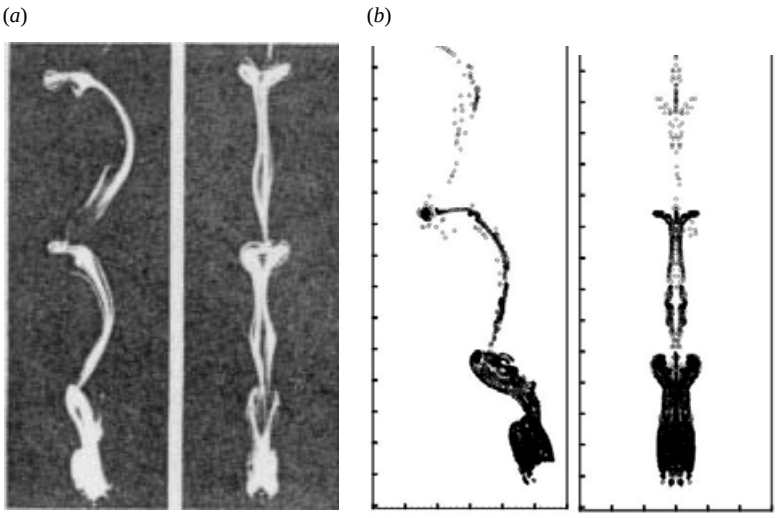

FIGURE 6. Streaks associated with shedding of hairpin vortices from a sphere: (*a*) experimental streaks from Sakamoto & Haniu (1990) for a fixed sphere; (*b*) our computational streaks for a sphere settling freely in a tube at $Re = 500$, $\lambda_a = 0.125$ and $t = 35$.

3.1.2. *Hairpin vortex*

The experiments of Achenbach (1974), Sakamoto & Haniu (1990, 1995) and Johnson & Patel (1999) showed that, for $300 < Re_T < 420$, the vortices are all shed with the same orientation, resulting in a ladder-like chain of overlapping hairpin-shaped structures (see figure 6*a*). For $Re_T > 420$, the vortices are shed as if the planes including them are rotating slowly and irregularly about the streamwise sphere axis. The hairpin vortices exist in the flow at Reynolds number up to the order of thousands (Achenbach 1974; Sakamoto & Haniu 1990). The vortex structures in the wake of a fixed sphere have been analysed numerically by Johnson & Patel (1999), Tomboulides & Orszag (2000) and Ploumhans *et al.* (2002). We now examine the vortex structures in our flows. A number of criteria for the identification of vortices have been proposed, among which the regions of complex eigenvalues of the velocity gradient tensor (Chong, Perry & Cantwell 1990), the Hessian of pressure (Jeong & Hussain 1995) and the imaginary part of complex eigenvalue of the velocity gradient tensor (Zhou *et al.* 1999) have been proved successful. Following Zhou *et al.* (1999), we use the iso-surface of λ_{ci}^2 to visualize the vortex structure, λ_{ci} being the imaginary part of the complex eigenvalue of the velocity gradient tensor.

In order to compare our results with experiments and other computations where the wall effect was not relevant, we consider a new case of $\lambda_a = 0.125$. The initial lateral position of the sphere is $(x_0, y_0) = (-2, 0)$ and Re is set to 500. Re_{max} of 575 is observed during the simulation. The particle tracers, the iso-surface of λ_{ci}^2 and the iso-surface of the streamwise vorticity at $t = 35$ are shown in figures 6, 7 and 8, respectively. From figures 7 and 8, the vortex structures are composed of a vortex loop located mainly in a plane perpendicular to the streamwise direction and two pairs of streamwise vortices. One pair of the streamwise vortices extends from the centre of the loop and the other is located between consecutive loops. The two pairs have opposite rotation directions. Clearly, the latter are responsible for the bending and kinking of the streaks between the loops in figure 6. Our streamwise vortex structures agree well with those obtained by Tomboulides & Orszag (2000) for $Re_T = 500$. From

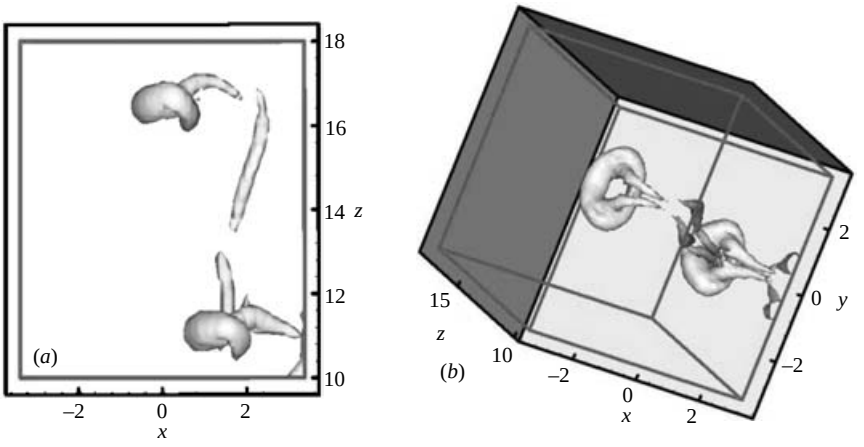

FIGURE 7. Vortex structures identified by an iso-surface of $\lambda_{ci}^2 = 0.0015$, around 2% of the maximum; (*a*) side view; (*b*) oblique view. $Re = 500$, $\lambda_a = 0.125$, $(x_0, y_0) = (-2, 0)$, and $t = 35$.

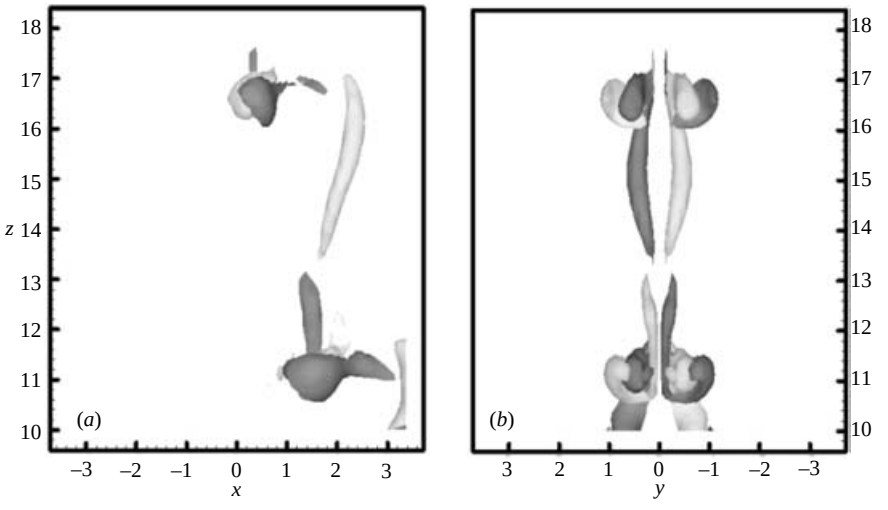

FIGURE 8. Iso-surfaces of the streamwise vorticity ω_z (*a*) (x, z)-plane view and (*b*) (y, z)-plane view. Dark surfaces indicate positive vorticity of 0.5 and light surfaces indicate negative vorticity of -0.5. $Re = 500$, $\lambda_a = 0.125$, $(x_0, y_0) = (-2, 0)$, $t = 40$.

figure 8, the distance between two consecutive loops is about 5.5 and this means that the Strouhal number is about 0.18, in good agreement with the experimental data of Sakamoto & Haniu (1990).

From our video of the vortex structures for $(Re, \lambda_a) = (400, 0.2)$, after shedding, the legs of the hairpin vortex retract, and in the meantime, a streamwise vortex pair with rotation direction opposite to that of the legs appears near them, as shown in figure 9*a*. In this case, the pair is much weaker than for the case of $Re = 500$, and the lower Reynolds number could be the reason. In addition, a vortex structure develops under the legs of the hairpin vortex and is connected to the hairpin vortex, making it ring-shaped (figures 7 and 9*a*). The new part, however, is much weaker than the hairpin head and therefore we still can take the entire vortex structure as

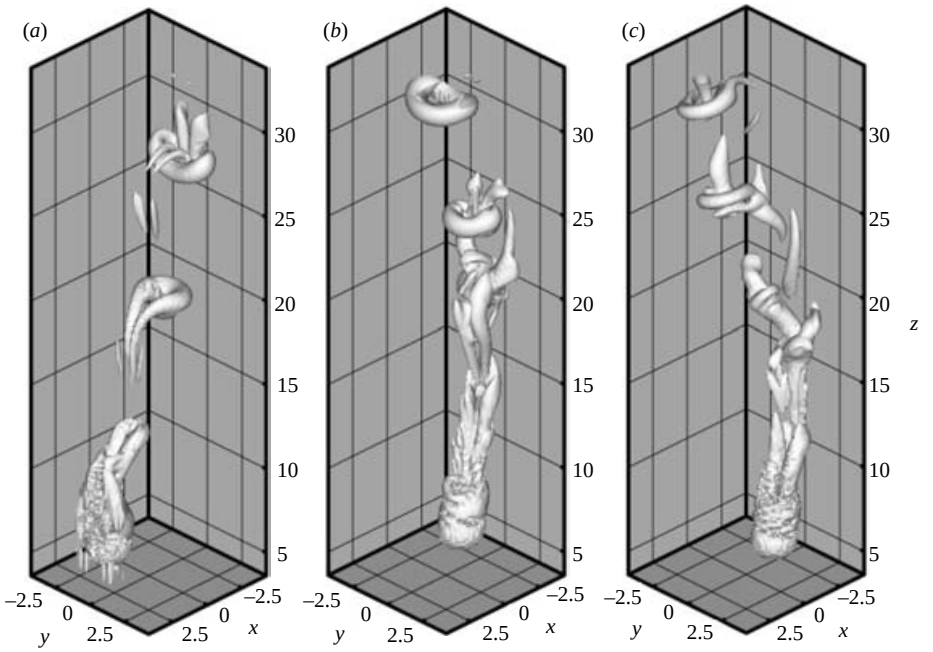

FIGURE 9. Vortex structures identified by an iso-surface of $\lambda_{ci}^2 = 0.0015$. (*a*) $t = 30$; (*b*) $t = 63$; and (*c*) $t = 148$. $(Re, \lambda_a) = (400, 0.2)$.

hairpin vortex. In Stage One, with the migration direction of the sphere reversed, the orientation of the hairpin vortex is also reversed. It is observed that the impact of the sphere on the wall results in intense shedding of the entire vortex sheet from the sphere, unlike the one-side shedding of the hairpin vortex. The change in the sphere migration direction and the rapid change in the sphere rotation mentioned earlier during the impact process are expected to be responsible for this kind of shedding. Although the shedding of the vortex sheet can affect the rotation of the sphere, we conjecture that the rapid change in the sphere rotation is mainly caused by the wall effect. The vortex shed during an impact cannot develop into a hairpin vortex (figure 9*b*), and the structure formed may differ for different impacts. In Stage Two, although the impact of the sphere on the wall is along a curved line (figure 2), its effect on the wake structure is almost as strong as in Stage One, in the sense that the wake structures shed during the impact period typically form into streamwise vortex structures and otherwise form into hairpin vortices (figure 9*c*). Due to the spiral motion and three-dimensional rotation of the sphere, all structures in Stage Two appear to be rotating.

3.2. *Migration of a sphere in the Poiseuille flow*

We are concerned with the motion of a slightly heavier sphere in a vertical tube filled with fluid moving upwards (upflow) and downwards (downflow), respectively. Unlike the sedimentation case above, the spheres always move in a plane in the present case because of small slip Reynolds numbers. Therefore, we use the radial position r to represent the lateral position of the sphere. The initial translational and angular velocities of the sphere are set to be zero.

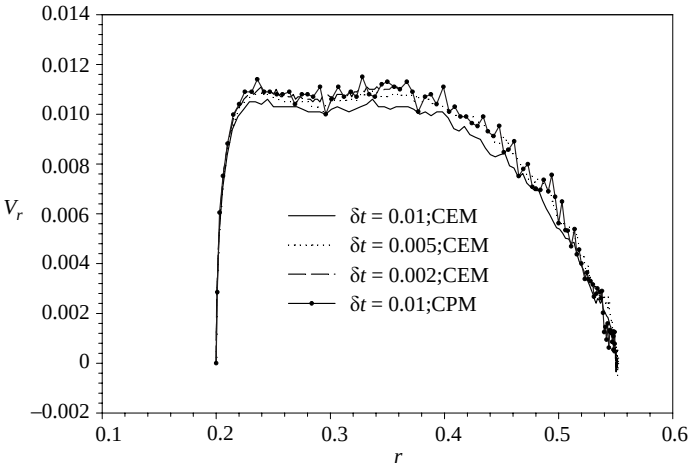

FIGURE 10. Convergence test for the migration rate of a sphere in an upflow at $Re_t = 100$, $\lambda_f = 0.0001$, $\lambda_a = 0.25$, $\rho_r = 1.001$ and $r_0 = 0.2$.

3.2.1. *Convergence test*

Our previous numerical experiments on the DLM method showed that its accuracy is relatively insensitive to the spatial resolution of the mesh, but the temporal convergence rate is relatively poor due to the use of the operator-splitting technique. In order to choose a reasonable value for the time step, a convergence test with different time steps was conducted for the migration rate of the sphere released from $r_0 = 0.2$ in upflow at $Re_t = 100$, $\lambda_f = 0.0001$, $\lambda_a = 0.25$ and $\rho_r = 1.001$. The results are shown in figure 10, from which we can see that the time step of 0.01 provides an essentially converged solution, particularly for the prediction of the equilibrium position, although a completely converged migration rate has not been achieved even at time step of 0.002. The migration rate calculated with the collocation element method (CEM) increases slightly with decreasing time step and is a little lower than that with the collocation point method (CPM) at the same time step value. The CE method and the time step of 0.01 are used for the following calculations.

3.2.2. *Role of the density ratio*

According to the theory of dimensional analysis, there are three dimensionless control parameters such as (ρ_r, Re, λ_a) for the sedimentation of a sphere in a tube and four parameters such as $(Re_t, \lambda_a, \lambda_f, \rho_r)$ for the motion of a sphere in a circular Poiseuille flow, respectively. However, the steady solution is independent of ρ_r since ρ_r appears only in the unsteady terms of equation (2.1), recalling that Fr defined in all cases contains the term $1/(\rho_r - 1)$. Moreover, the migration rate of a more dense sphere in a Poiseuille flow is found to be relatively insensitive to ρ_r, as shown in figure 11(*b*). Therefore, we only discuss the effects of Re_t, λ_a and λ_f on the motion of a slightly more dense sphere in Poiseuille flow, as Jeffrey & Pearson (1965) did for their experimental work. Note that Re and λ_f can reflect the effects of the density differences.

Equations (2.7)–(2.8) cannot handle the situation where the particle is neutrally buoyant. This difficulty has been overcome by Pan & Glowinski (2002) by modifying the original computational scheme. Another simple method is to take the numerical solution for a very small density difference as an approximation for the neutrally buoyant case. In fact, one is unlikely to encounter particles which are precisely

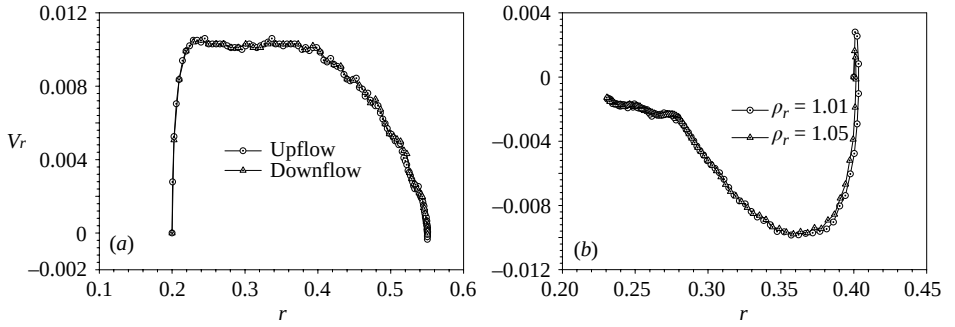

FIGURE 11. Migration rate at (*a*) $\lambda_f = 0.0001$, $\rho_r = 1.001$, showing that the sphere at the above parameter values is effectively neutrally buoyant; (*b*) $\lambda_f = 0.2$, upflow, showing that the density ratio is a relatively unimportant control parameter. $Re_t = 100$, $\lambda_a = 0.25$.

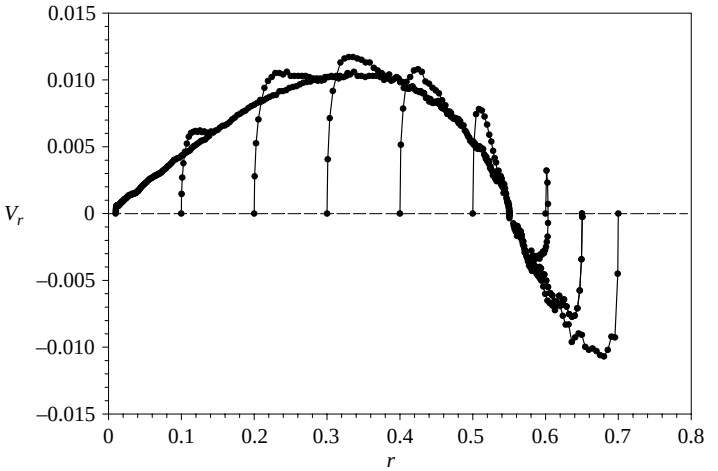

FIGURE 12. Radial velocities for neutrally buoyant spheres released from different radial positions in Poiseuille flow. $Re_t = 100$, $\lambda_a = 0.25$.

neutrally buoyant in practical problems. Figure 11 shows that the migration rates for the spheres moving upwards and downwards respectively at $\lambda_f = 0.0001$ and $\rho_r = 1.001$ are in perfect agreement, indicating that the sphere at the above parameter values is effectively neutrally buoyant. We will use $\lambda_f = 0.0001$ and $\rho_r = 1.001$ to investigate the motion of spheres in the neutrally buoyant case and $\rho_r = 1.01$ in the non-neutrally buoyant case, respectively. In the experiments of Jeffrey & Pearson (1965), the density differences in the non-neutrally buoyant case varied from 0.9% to 2.3%, as mentioned by Brenner (1966).

3.2.3. *Migration rate in the neutrally buoyant case*

Figure 12 shows the radial velocities for neutrally buoyant spheres released from different radial positions at $Re_t = 100$ and $\lambda_a = 0.25$. We can see that all velocities will eventually converge to a unique velocity profile, which is independent of the initial conditions of the spheres. For any sphere released from a position between the tube axis and the equilibrium position, the initial overshoot of the radial velocity is observed. A sphere released from a position closer to the wall than the equilibrium

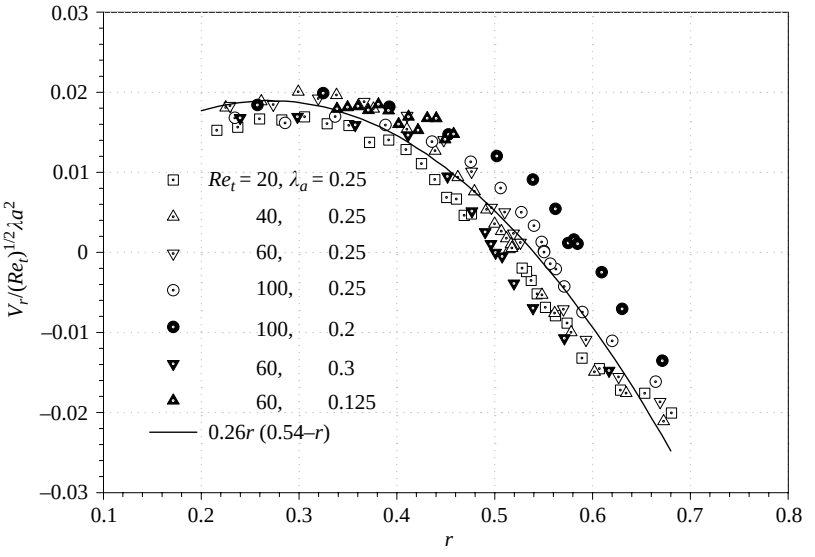

FIGURE 13. Radial velocities plotted as $V_r/\sqrt{Re_t}\lambda_a^2$ vs. radial position for the neutrally buoyant case in Poiseuille flow.

position initially drifts outward and its radial velocity approaches a unique velocity profile without any overshoot. These transient phenomena are dependent on Re_t and λ_a: for example, the overshoot is stronger at $Re_t = 200$ and $\lambda_a = 0.25$ (figure 14) and appears to vanish at $Re_t = 60$ and $\lambda_a = 0.125$. We are not interested in the transient behaviour of the sphere, but in the subsequent stage in which the radial velocity of the sphere becomes independent of its initial conditions.

The shape of velocity profile shown in figure 12 resembles the one observed in experiments: $r(r^* - r)$, where r^* denotes the equilibrium position (e.g. Segré & Silberberg 1962). The numerical velocity profile for $r < r^*$(about 0.55) is not symmetric about $r^*/2$, and the maximum velocity occurs for r larger than $r^*/2$.

Figure 13 plots the radial velocities at Re_t in the range of 20–100 and $\lambda_a = 0.2$–0.3. Clearly, the equilibrium position is closer to the wall at higher Re_t and lower λ_a, consistent with the observations of Karnis *et al.* (1966) who found that the equilibrium position was shifted closer to the tube axis as λ_a increased in their experiments at $Re_t \leqslant 1.1$ and was smaller than those reported by others (Segré & Silberberg 1962; Oliver 1962; Jeffrey & Pearson 1965) at larger Re_t and the same λ_a. Nevertheless, there exist Re_t and λ_a regimes in which the equilibrium position is insensitive to Re_t or λ_a. For example, at $\lambda_a = 0.25$, the equilibrium position is not sensitive to Re_t as it increases up to 150, as shown in figure 14.

Much attention has been paid to determining the exponents Re_t and λ_a appearing in the expression for the migration rate. Karnis *et al.* (1966) claimed that the exponent on λ_a depends on the value of λ_a because they noticed that the exponent is 4 as $\lambda_a \to 0$ (Rubinow & Keller 1961), equals on approximately 3 at small λ_a from both theory (Cox & Brenner 1966) and experimental results at $\lambda_a = 0.028$–0.153 (Segré & Silberberg 1962), and decreases to 2 at $\lambda_a = 0.25$–0.305 from their own experiment results. In all the theories and experiments mentioned above, the exponent on Re_t is unity. However, Jeffrey & Pearson (1965) found that their radial velocities at $Re_t = 11.2$–76.8 and $\lambda_a = 0.046$–0.089 were better correlated with $(Re_t)^{1/2}\lambda_a^2$ than with

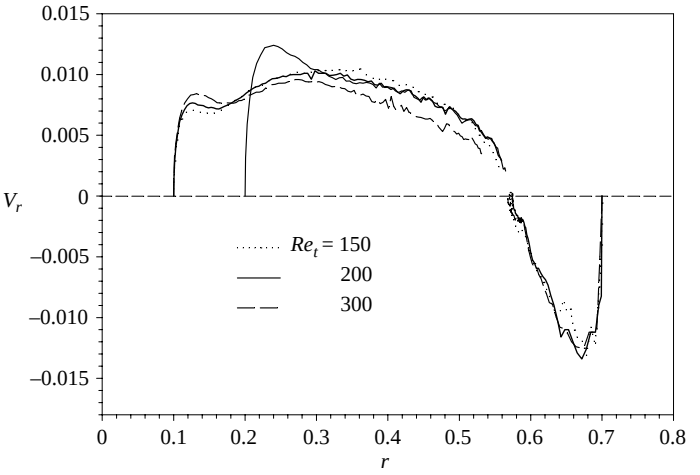

FIGURE 14. Radial velocities for neutrally buoyant spheres in Poiseuille flow at high tube Reynolds numbers and $\lambda_a = 0.25$, showing that the migration rate may decrease with increasing Re_t.

$Re_t\lambda_a^{2.84}$, which was presented by Segré & Silberberg for $Re_t = 2$–30 and $\lambda_a = 0.028$–0.153. Jeffrey & Pearson (1964) gave the radial velocity as

$$V_r = 0.35(Re_t)^{1/2}\lambda_a^2 r(r^* - r), \tag{3.2}$$

whereas Segré & Silberberg (1962) gave

$$V_r = 0.17Re_t\lambda_a^{2.84} r(r^* - r). \tag{3.3}$$

Jeffrey & Pearson (1964) reworked the original data of Segré & Silberberg (1962) and showed that their data could equally well be represented by an equation that is same as equation (3.2) but with coefficient 0.093 with roughly the same degree of precision as equation (3.3) (see also Brenner 1966). Figure 13 shows that

$$V_r = 0.26(Re_t)^{1/2}\lambda_a^2 r(0.54 - r) \tag{3.4}$$

can represent well our radial velocities for the parameter range covered.

At a fixed λ_a, there exists a value of the exponent on Re_t that can optimally correlate the data at two different Re_t, although perfect correlation is not possible due to different velocity profile shapes at different parameter values. The optimal exponent can be taken as an average one for that Re_t interval and if that interval is small enough, then it represents the exponent at that Re_t. If we highlight the correlation at the radial position of about 0.3, figure 13 reveals that the exponent of 1/2 is too small for $Re_t = 20$–40, good for $Re_t = 40$–60 and too large for $Re_t = 60$–100 at $\lambda_a = 0.25$. The exponent even becomes negative when Re_t exceeds 150, as indicated in figure 14. Similarly, figure 13 shows that the exponent of 2 in λ_a is too large for both $\lambda_a = 0.2$–0.25 at $Re_t = 100$ and $\lambda_a = 0.25$–0.3 at $Re_t = 60$, and appears to be good for $\lambda_a = 0.3$–0.125 at $Re_t = 60$. Calculations further reveal that the exponent of about 1.5 is good for $\lambda_a =$ 0.2–0.3. Therefore, from our results, the exponents on Re_t decrease with increasing Re_t, and the exponent for λ_a decreases with increasing λ_a. In addition, it seems that the exponent on λ_a decreases with increasing Re_t, taking into account the fact that Karnis *et al.* (1966) observed the exponent of 2 at $\lambda_a = 0.25$–0.305 and $Re_t \leqslant 1.1$, as mentioned earlier, and is about 1.5 at high Re_t according to our results.

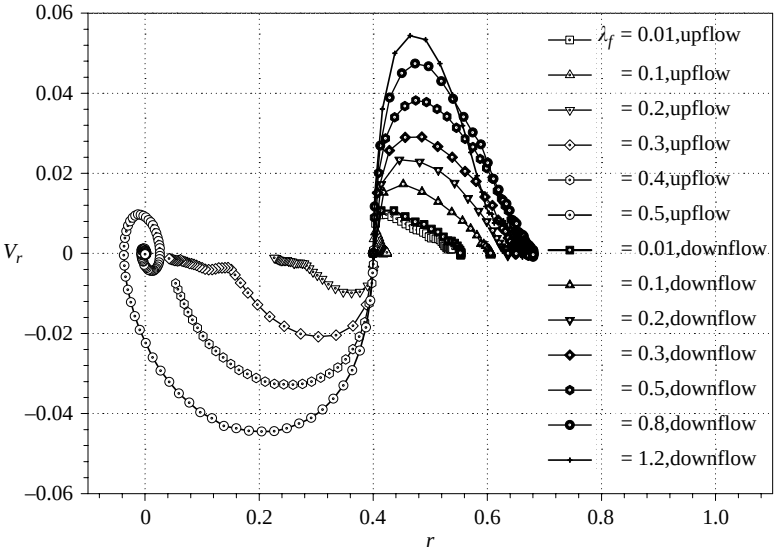

FIGURE 15. Radial velocities for more dense spheres released from $r_0 = 0.4$ at different λ_f. $Re_t = 100$, $\lambda_a = 0.25$.

3.2.4. *Migration rate in the non-neutrally buoyant case*

When the sphere is not neutrally buoyant, a general conclusion is that a leading one migrates towards the tube wall and a lagging one migrates towards the tube axis. Nevertheless, strictly speaking, the stable equilibrium position for a leading sphere is just closer to the wall than that for a corresponding neutrally buoyant sphere, and the sphere would migrate inward if released from a position near the wall, as observed by Karnis *et al.* (1966). In addition, it is conceivable that a very small density difference will not lead to a significant departure of the equilibrium position from the one in the corresponding neutrally buoyant system. Figure 15 shows the radial velocities of a denser sphere released from $r_0 = 0.4$ at different λ_f, $Re_t = 100$ and $\lambda_a = 0.25$. The spheres at $\lambda_f = 0.01$ are almost neutrally buoyant. In upflow, r^* shifts closer to the tube axis with increasing λ_f, and the sphere approaches the tube axis with overshoot as λ_f increases up to 0.5, a phenomenon that was first observed by Denson *et al.* (1966). In downflow, r^* shifts closer to the wall with increasing λ_f till λ_f reaches a critical value where the extreme position is attained, and then the equilibrium position begins to shift towards the tube axis as λ_f increases. According to figure 15, the critical λ_f and the extreme position are 0.8 and 0.68, respectively. Qualitatively the same results have been reported by Feng *et al.* (1994*b*), Huang *et al.* (1997) and Yu *et al.* (2002*a*) for a circular particle in a plane Poiseuille flow. Nevertheless, a leading circular particle at a moderately large density ratio (equivalent to λ_f here) was observed to approach the channel centreline, whereas figure 15 shows that an equilibrium position in the vicinity of the tube axis is much more difficult, if possible, for a leading sphere to reach, and r^* of less than 0.3 was not observed by us even at $\lambda_f = 5$. This may explain why the equilibrium position in the vicinity of the tube axis for a leading sphere in Poiseuille flow has never been reported in the experimental works.

As shown in figure 15, the migration rates in the non-neutrally buoyant system are much higher than in the neutrally buoyant system, allowing us to examine them at smaller λ_a. The radial velocities for denser spheres in downflow and in upflow at

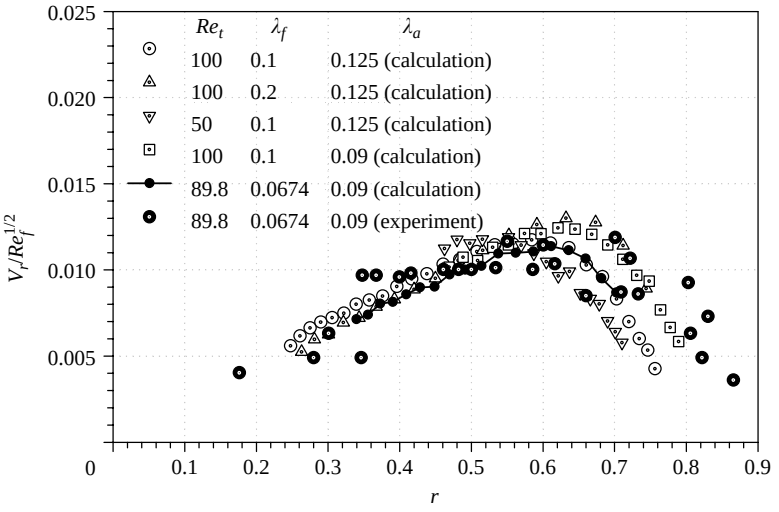

FIGURE 16. Radial velocities plotted as $V_r/\sqrt{Re_f}$ vs. radial position for more dense spheres in downflow. The experimental data are from Jeffrey & Pearson (1965).

$\lambda_a = 0.09$–0.125 are depicted in figure 16 and figure 17, respectively. The shape of the velocity profiles for denser spheres in downflow bears a resemblance to that in the neutrally buoyant system. From figure 16, the equilibrium position shifts closer to the wall as λ_a decreases, Re_t increases, or λ_f increases. Using the same method as described earlier for determining the optimal exponents in the neutrally buoyant case, $V_r/(\lambda_a^{1/2} Re_t^{1/2} \lambda_f^{1/2})$, i.e. $V_r/Re_f^{1/2}$ is found to provide a good correlation of the radial velocities at $r = 0.5$–0.6 and $(Re_t, \lambda_f, \lambda_a) = (100, 0.1, 0.125)$, $(100, 0.2, 0.125)$, $(50, 0.1, 0.125)$ and $(100, 0.1, 0.09)$. It is encouraging to find that this scaling is same as the one revealed by the experimental results of Jeffrey & Pearson (1965) and can account well for the case of $(Re_t, \lambda_f, \lambda_a) = (89.8, 0.0674, 0.09)$. Moreover, our numerical results are in quantitative agreement with their experimental data, as shown in figure 16. The radial velocities at $Re_t = 100$, $\lambda_a = 0.25$ and $\lambda_f = 0.1$–0.8 for denser spheres in downflow given in figure 15 can also be well-correlated by using $V_r/\lambda_f^{1/2}$.

From figure 17, the stable equilibrium position for a denser sphere in upflow is generally the tube axis as λ_a decreases down to 0.125. The velocity profile as a linear function of r was predicted by the theory of Rubinow & Keller (1961) and was used by Jeffrey & Pearson (1964) for correlating their experimental data (see also Brenner 1966). However, figure 17 reveals that the magnitude of the radial velocity does not vary quickly with r for $r > 0.4$ for the case of $(Re_t, \lambda_f, \lambda_a) = (115, 0.0527, 0.09)$, and with increasing λ_f the velocity profile even becomes a quadratic-like function with the peak occurring closer to the tube axis. It is understandable that Jeffrey & Pearson (1965) chose a linear function for correlating their data, since most of their data were located at $r < 0.6$, and the case of $\lambda_a = 0.046$ was also considered for correlation, where the velocity profile could be much different from the case of $\lambda_a = 0.09$. It is difficult to determine an unambiguous velocity profile from their relatively scattered data. The scaling $V_r/\lambda_f^{1.1} Re_t^{0.4}$ is obtained by considering the correlation of our radial velocities at $r = 0.4$–0.6 and $(Re_t, \lambda_f, \lambda_a) = (100, 0.1, 0.125)$, $(100, 0.2, 0.125)$, $(50, 0.1, 0.125)$ and $(100, 0.1, 0.09)$. It is surprising to find that λ_a does not play a role in the scaling. Figure 17 shows that the radial velocity at $(Re_t, \lambda_f, \lambda_a) = (115, 0.0527, 0.09)$ is captured

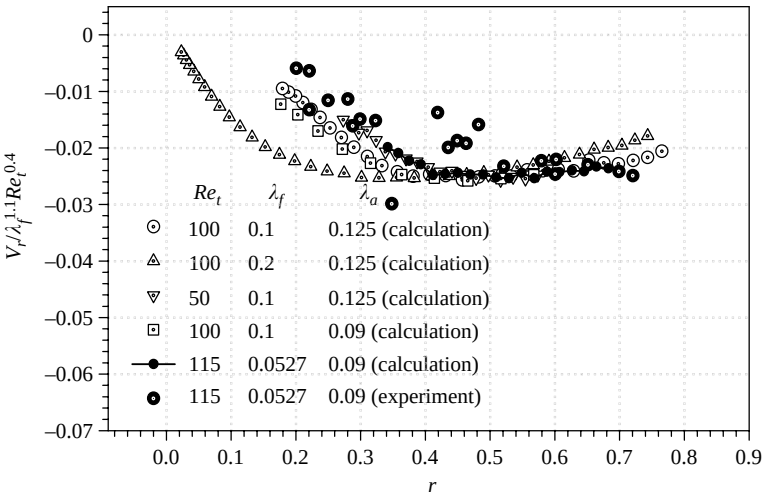

FIGURE 17. Radial velocities plotted as $V_r/\lambda_f^{1.1}Re_t^{0.4}$ vs. radial position for more dense spheres in upflow. The experimental data are from Jeffrey & Pearson (1965).

by the scaling $V_r/\lambda_f^{1.1}Re_t^{0.4}$ and is in quantitative agreement with the experimental data.

3.2.5. *Angular velocity and axial velocity*

We inspect the behaviour of the angular and axial velocities of neutrally buoyant spheres at $(Re_t, \lambda_a) = (100, 0.25), (100, 0.2)$ and $(20, 0.25)$ respectively, and non-neutrally buoyant spheres at $(Re_t, \lambda_f, \lambda_a) = (100, 0.1, 0.125)$ in upflow and downflow respectively. The results for angular and axial velocities are shown in figures 18 and 19 respectively. For convenience, the directions of both angular velocities and axial velocities are not considered. $(Re_t, \lambda_a) = (100, 0.25)$ is the only case in which the data are composed of those for several particles released from different radial positions.

Jeffrey & Pearson (1965) observed that the angular velocities of neutrally buoyant spheres were systematically smaller than the theoretically predicted one $\Omega = r$ and the angular velocities of non-neutrally buoyant spheres were statistically around $\Omega = r$, irrespective of whether the spheres lead or lag the entraining fluids. Consistent with their observations, all of our angular velocities of neutrally buoyant spheres are smaller than $\Omega = r$ (figure 18). Our results show that the effects of Re_t and λ_a on the angular velocities are appreciable. At $(Re_t, \lambda_a) = (100, 0.25)$, the angular velocity is approximately $\Omega = 0.91r$, and the data at lower Re_t and λ_a are closer to $\Omega = r$, particularly for the case of $(Re_t, \lambda_a) = (20, 0.25)$ (figure 18). It is known that the fluid inertia results in the rotation of a particle lagging the rotation of the fluid in a simple shear flow (e.g. Ding & Aidun 2000), and our results indicate that the ratio of the sphere rotation to the local fluid rotation in a Poiseuille flow is approximately a constant. For a non-neutrally buoyant sphere in downflow at $(Re_t, \lambda_f, \lambda_a) = (100, 0.1, 0.125)$, the angular velocity is slightly smaller than $\Omega = r$. By contrast, the angular velocity in the case of upflow is lower than $\Omega = r$ at r greater than about 0.5 and higher than $\Omega = r$ at r less than about 0.5, as shown in figure 18. The departure of the angular velocity from $\Omega = r$ is expected to be more significant at higher λ_f, and the overshoot of the angular velocity at the tube axis is observed in the case of $(Re_t, \lambda_f, \lambda_a) = (100, 0.5, 0.25)$, accompanied by the aforementioned overshoots of the radial position and the radial velocity shown in figure 15.

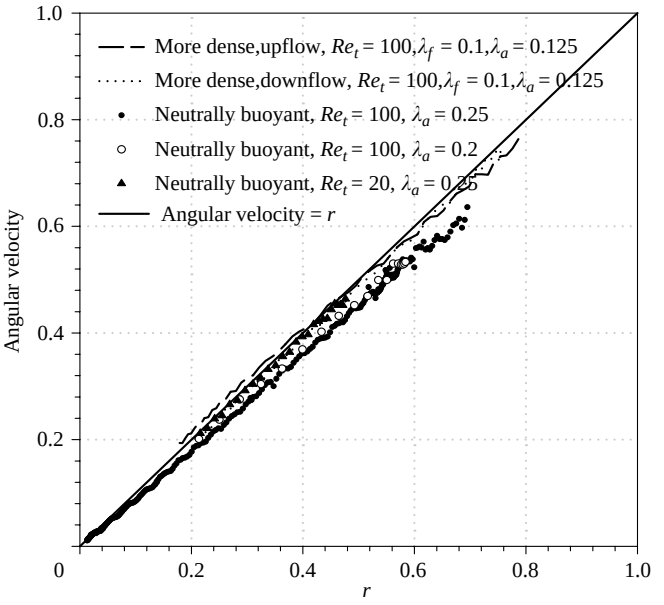

FIGURE 18. Angular velocities of the spheres in Poiseuille flow. The directions of the angular velocities are not considered for convenience.

Two types of functions were used by Jeffrey & Pearson (1965) to fit their axial velocities. Type I is $U_z = U_r + c$ and type II is $U_z = cU_r$, here U_r being the undisturbed fluid velocity, i.e. $U_r = 1 - r^2$, and c being a constant. In type I the slip velocity is assumed unchanged with r, and in type II the slip velocity decreases as r increases. The axial velocity data presented by Jeffrey & Pearson (1965) in downflow agreed with type II, but the data in upflow were so scattered that they were unable to decide which type was better. Our results confirm that type II is better for the downflow case and reveal that type I is better for the upflow case, as can be seen from figure 19. It is worth noting that $U_r = 1 - r^2$ cannot represent accurately the undisturbed fluid velocity in our simulations, since we employ the pressure-gradient-invariant approach and a slight change of the flow flux due to the presence of the sphere does exist, which becomes more pronounced as λ_f or the simulation duration increases. As a result, spheres released from different radial positions for a certain set of parameters have their own axial velocity profiles; a unique and common velocity profile cannot be obtained, as is shown in figure 19 from which we can see that for the case of $(Re_t, \lambda_a) = (100, 0.25)$ a combination of three sections of data demarcated by $r \approx 0.3$ and $r \approx 0.55$ cannot form a smooth curve. Taking this into account, the axial velocities in upflow and downflow in a system with fixed flow flux would even agree better with their corresponding types than shown in figure 19, respectively. Figures 12 and 18 show that the radial velocities and the angular velocities are much less insensitive to the small change of the flow flux than the axial velocities, since the curves can be connected smoothly.

Figure 19 shows that the axial velocities in the neutrally buoyant case are in better agreement with type I than type II, and the slip velocity is smaller at lower λ_a, which is in qualitative agreement with equation (2.25). The effect of Re_t on the axial velocity is found to be small, since the data at $(Re_t, \lambda_a) = (100, 0.25)$ and $(20, 0.25)$ are close to each other, the latter not being plotted in figure 19 for clarity.

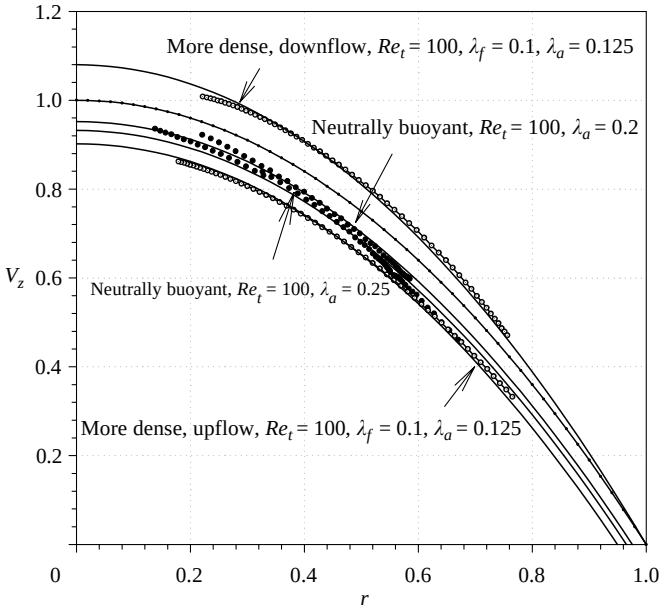

FIGURE 19. Axial velocities of the spheres in Poiseuille flow. The directions of the axial velocities are not considered for convenience. The solid lines are the best fits to the data with the function $c(1-r^2)$ or $(1-r^2)+c$, c being a constant.

3.2.6. *Lift force*

We have shown that the Magnus effect plays an important role in the lateral motion of a sphere in the sedimentation case. The Magnus effect is related to the rotation of a particle. It has been recognized that the rotation of a fluid can also provide a lift force on a particle known as the Saffman force. Saffman (1965) analysed the lift force on a sphere in a linear unbounded shear flow with the assumptions that $Re_{slip} \ll 1$, $Re_{sh} \ll 1$, and $\epsilon = Re_{slip}/\sqrt{Re_{sh}} \ll 1$, here Re_{slip} being the slip Reynolds number defined in (2.24), and Re_{sh} the shear Reynolds number defined by $Re_{sh} = \rho_f \dot{\gamma}(2a)^2/\eta$ where $\dot{\gamma}$ is the shear rate. He derived the following expression:

$$\boldsymbol{F}_{sa1} = 6.46a^2(\eta\rho_f)^{1/2}|\boldsymbol{\omega}_f|^{-1/2}(\boldsymbol{\omega}_f \times \boldsymbol{U}_s), \tag{3.5}$$

where $\boldsymbol{U}_s$ is the slip velocity of the sphere with respect to the fluid, and $\boldsymbol{\omega}_f$ represents the vorticity (rotation) of the fluid $\nabla \times \boldsymbol{u}$, $\boldsymbol{u}$ being the fluid velocity; for a shear flow, $|\boldsymbol{\omega}_f|$ is actually the shear rate $\dot{\gamma}$. The results of Saffman (1965) further revealed that the effect of the sphere rotation is not important to the lift force unless the angular velocity of the sphere is greater than the shear rate. MacLaughlin (1991) extended Saffman's analysis to allow the slip Reynolds number to exceed unity and found that the lift force decreases with increasing ϵ. From the results of MacLaughlin (1991) for $0.05 \leqslant \epsilon \leqslant 10$, Mei (1992) obtained a modified lift force $\boldsymbol{F}_{sa2}$ in the following form:

$$\frac{\boldsymbol{F}_{sa2}}{\boldsymbol{F}_{sa1}} \approx 0.3\left\{1 + \tanh\left[2.5\log_{10}\left(\frac{1}{\epsilon} + 0.191\right)\right]\right\}\left\{0.667 + \tanh\left[6\left(\frac{1}{\epsilon} - 0.32\right)\right]\right\}. \tag{3.6}$$

$\boldsymbol{F}_{sa2}$ was found in very good agreement with the numerical results of Kurose & Komori (1999) for $Re_{slip} < 5$.

The Saffman force (3.5) or (3.6) is derived from a linear unbounded shear flow, and consequently is not valid for evaluating the lift force on a sphere in a general

shear flow. For example, it cannot explain why a neutrally buoyant sphere migrates to the Segré–Silberberg equilibrium position in Poiseuille flow and to the centreplane in Couette flow, since the Saffman force based on the local shear rate is always directed toward the high-velocity side of the sphere due to the fact that a neutrally buoyant particle always lags the fluid. The results of the perturbation theory (e.g. Ho & Leal 1974) revealed that the curvature of the velocity profile and the wall effect are important to the aforementioned sphere migrations. However, the Saffman effect should be important to the one-way migration of a non-neutrally buoyant sphere, since the Saffman force and the migration have the same directions in both cases. In the following, we attempt to make a quantitative comparison between the Saffman force and the lift force on a sphere.

Consider the case of $(Re_t, \lambda_f, \lambda_a) = (100, 0.1, 0.125)$. In the Poiseuille flow case, $Re_{slip} = 2|\boldsymbol{U}_s|\lambda_a Re_t$, $Re_{sh} = \dot{\gamma} Re_s = 4\lambda_a^2 Re_t \dot{\gamma}$, and $\epsilon = \sqrt{Re_t}|\boldsymbol{U}_s|/\sqrt{\dot{\gamma}}$, $\boldsymbol{U}_s$ and $\dot{\gamma}$ being the dimensionless slip velocity and shear rate. $\|\boldsymbol{U}_s\|$ is determined from our computations (figure 19) and $\dot{\gamma} = 2r$. For the present problem, typically, $|\boldsymbol{U}_s| = 0.1$ and $\dot{\gamma} = 1$, and we then obtain $Re_{slip} = 2.5$, $Re_{sh} = 6.25$, and $\epsilon = 1$, hence, the Saffman force should be calculated with the second formulation (3.6). The dimensionless form of (3.5) is

$$\boldsymbol{F}_{sa1} = \frac{6.46\lambda_a^2}{\sqrt{Re_t}} |\boldsymbol{\omega}_f|^{-1/2} (\boldsymbol{\omega}_f \times \boldsymbol{U}_s). \tag{3.7}$$

The scale of a force is $\rho_f U_m^2 R^2$. For convenience, the dimensionless quantities appearing in this section are written in the same form as their dimensional counterparts.

A lift force drives a sphere to migrate radially, and at the same time the sphere undergo a drag due to its migration; therefore the migration rate is determined from the net force, i.e.

$$M \frac{\mathrm{d}\boldsymbol{V}_r}{\mathrm{d}t} = \boldsymbol{F}_t = \boldsymbol{F}_l - \boldsymbol{F}_d, \tag{3.8}$$

where $\boldsymbol{F}_t$, $\boldsymbol{F}_l$ and $\boldsymbol{F}_d$ denote the total radial force, the lift force and the radial drag force, respectively. Considering that the Stokes drag law is used to calculate the drag force in the perturbation theory (e.g. see Asmolov 1999), we here use the standard drag law to compute the drag force, i.e.

$$\boldsymbol{F}_d = 6\pi a \eta f \boldsymbol{V}_r, \tag{3.9}$$

where f is the drag factor arising from the fluid inertial effect. In other words, the drag force is calculated with the point-particle model. It should be noted that the drag force evaluated this way is not an accurate one for the Poiseuille flow studied, since the shear and wall effects are not considered in the standard drag law. But the error is expected to be insignificant except in the vicinity of the wall.

Since the radial velocities are smaller by a factor of one order in magnitude than the axial slip velocities (figures 16, 17 and 19), we take the axial slip velocities as the total slip velocities for evaluating the particle Reynolds number. Since the typical Re_{slip} is 2.5 for the present problem, we choose $f = (1 + \frac{3}{16} Re_{slip})$, which is valid for Re_{slip} up to 5.0 (e.g. see Crowe, Sommerfeld & Tsuji 1998). The dimensionless form of the particle inertial force (i.e. the total radial force) is

$$\boldsymbol{F}_t = \frac{4}{3}\pi \rho_r \lambda_a^3 \frac{\mathrm{d}\boldsymbol{V}_r}{\mathrm{d}t},$$

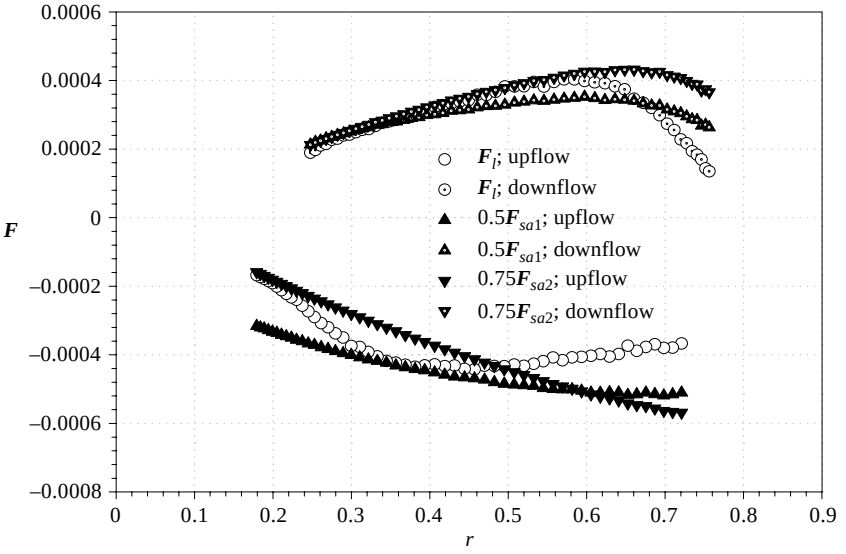

FIGURE 20. Comparison between Saffman forces $\boldsymbol{F}_{sa1}$ and $\boldsymbol{F}_{sa2}$ and lift force $\boldsymbol{F}_l$ on a more dense sphere in Poiseuille flow at $(Re_t, \lambda_f, \lambda_a) = (100, 0.1, 0.125)$.

and that of the drag force is

$$\boldsymbol{F}_d = \frac{6\pi\lambda_a f \boldsymbol{V}_r}{Re_t}.$$

The ratio of the former to the latter in magnitude is

$$\frac{2}{9}\frac{\rho_r \lambda_a^2 Re_t}{f}\frac{\mathrm{d}V_r}{\mathrm{d}r}.$$

The coefficient $\frac{2}{9}\rho_r\lambda_a^2 Re_t/f$ is actually Stokes number characterizing the particle inertia or the response time of the particle to the flow, and its value is around 0.24 if we consider $\rho_r = 1.01$, $\lambda_a = 0.125$, $Re_t = 100$ and $Re_{slip} = 2.5$. $\mathrm{d}V_r/\mathrm{d}r$ can be estimated from figures 16 and 17, and we find that the particle inertial force is almost two orders in magnitude smaller than the drag force. As a result, the lift force approximately equals the drag force, i.e.

$$\boldsymbol{F}_l = \frac{6\pi\lambda_a f \boldsymbol{V}_r}{Re_t}.$$

The small particle inertia explains why the radial velocities for the spheres released from different radial positions change rapidly at initial times and then converge to a unique velocity profile, as shown in figure 12.

The calculated Saffman and lift forces are plotted in figure 20. The lift forces are smaller than the Saffman forces in both cases, particularly in the vicinity of the tube wall, where, however, the differences can be reduced to some extent by the consideration of the wall effect on the drag forces. One should not use the Saffman formula to compute the lift force, but from the physical point of view the Saffman effect is expected to be responsible for the one-way migration of a non-neutrally buoyant sphere.

Next, we consider the effect of sphere rotation on the lift force. It was observed experimentally that, for the neutrally buoyant case, the equilibrium position of a non-rotating sphere is closer to the tube axis than that of a freely rotating sphere

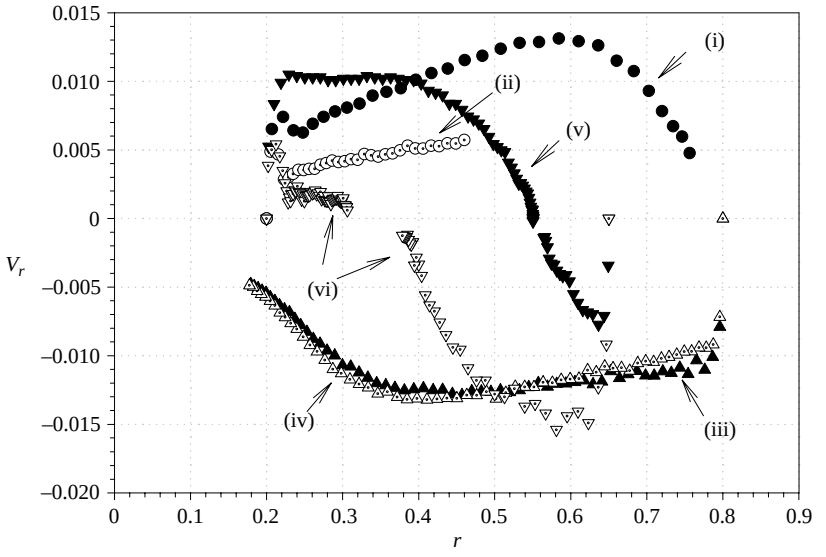

FIGURE 21. Effects of sphere rotation on the radial velocities. (i) more dense, downflow, freerotation; (ii) more dense, downflow, norotation; (iii) more dense, upflow, freerotation; (iv) more dense, upflow, norotation; (v) neutrally buoyant, free rotation; (vi) neutrally buoyant, norotation. For the neutrally buoyant case, $(Re_t, \lambda_a) = (100, 0.25)$, and for the non-neutrally buoyant case, $(Re_t, \lambda_f, \lambda_a) = (100, 0.1, 0.125)$.

(Oliver 1962). Patankar *et al.* (2001*a*) studied numerically the lift-off of a heavier circular particle in a horizontal two-dimensional Poiseuille flow, and found that a non-rotating particle rises further than a freely rotating one. Figure 21 compares the radial velocities of free-rotating and non-rotating spheres for the non-neutrally buoyant case of $(Re_t, \lambda_f, \lambda_a) = (100, 0.1, 0.125)$ and the neutrally buoyant case of $(Re_t, \lambda_a) = (100, 0.25)$. It is surprising to find that the suppression of the rotation produces significantly larger additional lift forces pointing to the tube axis on the spheres in the neutrally buoyant and more-dense-downflow cases, whereas it has a negligible effect on the migration of the more dense sphere in upflow, although the results for the neutrally buoyant case are in qualitative agreement with the experiments (Oliver 1962) and the numerical results of Patankar *et al.* (2001*a*). The Magnus effect is usually applied to the analysis of the lift force on a particle rotating in a homogeneous flow, and Crowe *et al.* (1998) suggested that it can be applied to a shear flow by replacing the angular velocity of the particle with the angular slip velocity. But apparently it cannot explain the above observations.

We conclude that the effects of the curvature of the velocity profile, the wall and the sphere rotation on the lift force on a sphere in a Poiseuille flow are very subtle, depending on whether the sphere is neutrally buoyant, more dense or less dense than the fluid, and therefore it would be difficult to establish general formulae to measure lift forces for the point-particle model by the separate consideration of these effects.

4. Conclusions

We have presented a new computational scheme for the DLM method that is obtained by replacing the previously used finite element method with a half-staggered finite difference method to solve the fluid-flow sub-problem. With the new scheme, we

have examined the sedimentation of a sphere and the radial migration of a sphere in Poiseuille flow in a vertical tube. The main conclusions in the sedimentation case are:

(*a*) At high Re_T where shedding of vortices takes place, a sphere takes up a spiral trajectory that is closer to the tube wall than the tube axis.

(*b*) The rotation motion and the lateral motion of a sphere are highly correlated through the Magnus effect. The Magnus force is an important, but not the sole, driving force for the lateral motion of the sphere at relatively high Reynolds numbers.

(*c*) For $Re_T > 400$, the standard vortex structures in the wake of a sphere are composed of a loop mainly located in a plane perpendicular to the streamwise direction and two streamwise vortex pairs. Due to the Kelvin–Helmholtz instability, the vortex sheet rolls up and is shed into the hairpin vortex. When moving downstream, the legs of the hairpin vortex retract and a streamwise vortex pair with rotation opposite to that of the legs form between the loops in the meantime.

(*d*) At Re_T around 400, the wake structures shed during the impact of the sphere on the wall typically form into streamwise vortex structures and otherwise form into hairpin vortices when the sphere spirals down.

The main conclusions in the Poiseuille flow case are:

(*a*) For the neutrally buoyant case, the equilibrium position is closer to the tube wall at higher Re_t and λ_a; however, there exists a critical Re_t above which the equilibrium position is insensitive to Re_t for a fixed λ_a.

(*b*) For the neutrally buoyant case, the exponents on Re_t decrease with increasing Re_t, and the exponent on λ_a decreases with increasing λ_a. $V_r = 0.26(Re_t)^{1/2}\lambda_a^2 r(0.54-r)$ can represent well the radial velocities at $Re_t = 20$–100 and $\lambda_a = 0.2$–0.3. The exponent on Re_t can be negative for large Re_t.

(*c*) For the neutrally buoyant case, the angular velocity ratio of the sphere to the local fluid is almost a constant. At $(Re_t, \lambda_a) = (100, 0.25)$, the angular velocity of the sphere is approximately $\Omega = 0.91r$, and the angular velocities at lower Re_t and λ_a are closer to $\Omega = r$.

(*d*) For the case of a more dense sphere in downflow, the equilibrium position shifts closer to the wall with increasing λ_f till the extreme position is attained, and then the equilibrium position begins to shift towards the tube axis as λ_f increases, but an equilibrium position in the vicinity of the tube axis is not observed at moderately large λ_f.

(*e*) For the case of a more dense sphere in downflow and the parameter range of $Re_t = 50$–100, $\lambda_f = 0.1$–0.2 and $\lambda_a = 0.09$–0.125, a scaling $V_r/Re_f^{1/2}$ is obtained for the correlation of the radial velocities.

(*f*) For the case of a more dense sphere in downflow and at $(Re_t, \lambda_f, \lambda_a) = (100, 0.1, 0.125)$, the angular velocity is very slightly smaller than $\Omega = r$ and the slip velocity decreases generally in the form of $1 - r^2$ as r increases.

(*g*) For the case of a more dense sphere in upflow and the parameter range of $Re_t = 50$–100, $\lambda_f = 0.1$–0.2 and $\lambda_a = 0.09$–0.125, a scaling $V_r/\lambda_f^{1.1}Re_t^{0.4}$ is obtained for the correlation of the radial velocities, whose profile is not a linear function of r.

(*h*) For the case of a more dense sphere in upflow and at $(Re_t, \lambda_f, \lambda_a) = (100, 0.1, 0.125)$, the angular velocity is lower than $\Omega = r$ at r greater than about 0.5 and higher than $\Omega = r$ at r less than about 0.5, and the slip velocity remains almost constant as the sphere migrates towards the tube axis.

(*i*) The Saffman force is larger than the lift force on a non-neutrally buoyant sphere, but the effect is expected to be important to the one-way migration.

(*j*) The suppression of the sphere rotation produces significant large additional lift forces pointing to the tube axis on the spheres in the neutrally buoyant and

more-dense-downflow cases, whereas it has a negligible effect on the migration of the more-dense sphere in upflow.

We wish to thank Professor Yurun Fan and Professor Xijun Fan for helpful discussions, and the referees for valuable suggesions and comments. The first author gratefully acknowledges IPRS from the Australian government and IPA from the University of Sydney for support of his study. The computations were performed on the workstations at National University of Singapore.

REFERENCES

Achenbach, E. 1974 Vortex shedding from spheres. *J. Fluid Mech.* **62**, 209–221.

Aidun, C. K., Lu, Y. & Ding, E.-J. 1998 Direct analysis of particulate suspensions with inertia using the discrete Boltzmann equation. *J. Fluid Mech.* **373**, 287–311.

Asmolov, E. S. 1999 The inertial lift on a spherical particle in a plane Poiseuille flow at large channel Reynolds number. *J. Fluid Mech.* **381**, 63–87.

Brady, J. F. & Bossis, G. 1988 Stokesian dynamics. *Annu. Rev. Fluid Mech.* **20**, 111–157.

Brenner, H. 1966 Hydrodynamic resistance of particles at small Reynolds numbers. *Adv. Chem. Engng* **12**, 287–438.

Cherukat, P., McLaughlin, J. B. & Dandy, D. S. 1999 A computational study of the inertial lift on a sphere in a linear shear flow field. *Intl J. Multiphase Flow* **25**, 15–33.

Choi, H. G. & Joseph, D. D. 2001 Fluidization by lift of 300 circular particles in plane Poiseuille flow by direct numerical simulation. *J. Fluid Mech.* **438**, 101–128.

Chong, M. S., Perry, A. E. & Cantwell, B. J. 1990 A general classification of three-dimensional flow fields. *Phys. Fluids* A **2**, 765–777.

Clift R., Grace, J. R. & Weber, M. E. 1978 *Bubbles, Drops, and Particles.* Academic.

Cox, R. G. & Brenner, H. 1968 The lateral migration of solid particles in Poiseuille flow. Part 1: Theory. *Chem. Engng Sci.* **23**, 147–173.

Cox, R. G. & Mason, S. G. 1971 Suspended particles in fluid flow through tubes. *Annu. Rev. Fluid Mech.* **3**, 291–316.

Crowe, C., Sommerfeld, M. & Tsuji, Y. 1998 *Multiphase Flows with Droplets and Particles.* CRC Press.

Dandy, D. S. & Dwyer, H. A. 1990 A sphere in shear flow at finite Reynolds number: effect of shear on particle lift, drag and heat transfer. *J. Fluid Mech.* **216**, 381–410.

Denson, C. D., Christiansen, E. B. & Salt, D. L. 1966 Particle migratoin in shear fields. *AIChE J.* **12**, 589.

Ding, E.-J. & Aidun, C. K. 2000 The dynamics and scaling law for particles suspended in shear flow with inertia. *J. Fluid Mech.* **423**, 317–344.

Feng, J., Hu, H. H. & Joseph, D. D. 1994*a* Direct simulation of initial value problems for the motion of solid bodies in a Newtonian fluid. Part 1. Sedimentation. *J. Fluid Mech.* **261**, 95–134.

Feng, J., Hu, H. H. & Joseph, D. D. 1994*b* Direct simulation of initial value problems for the motion of solid bodies in a Newtonian fluid. Part 2. Couette and Poiseuille flows. *J. Fluid Mech.* **277**, 271–301.

Francis, A. W. 1933 Wall effect in falling ball method for viscosity. *Physics* **4**, 403–406.

Glowinski, R. 2003 Finite element methods for incompressible viscous flow. In *Handbook of Numerical Analysis*, Vol. IX (ed. P. G. Ciarlet & J. L. Lions), pp. 3–1176. North-Holland.

Glowinski, R., Hesla, T. I., Joseph, D. D., Pan, T.-W. & Periaux, J. 1997 Distributed Lagrange multiplier methods for particulate flows. In *Computational Science for the Twenty-First Century* (ed. M.-O. Bristeau, G. Etgen, W. Fitzgibbon, J. L. Lions, J. Periaux & M. F. Wheeler), pp. 270–279. Wiley.

Glowinski, R. Pan, T.-W., Hesla, T. I. & Joseph, D. D. 1999 A distributed Lagrange multiplier/fictitious domain method for particulate flows. *Intl J. Multiphase Flow* **25**, 755–794.

Glowinski, R., Pan, T.-W., Hesla, T. I., Joseph, D. D. & Periaux, J. 2001 A fictitious domain approach to the direct numerical simulation of incompressible viscous flow past moving rigid bodies: Application to particulate flow. *J. Comput. Phys.* **169**, 363–426.

Ho, B. P. & Leal, L. G. 1974 Inertial migration of rigid spheres in two-dimensional unidirectional flows. *J. Fluid Mech.* **65**, 365–400.

Hogg, A. J. 1994 The inertial migration of non-neutrally buoyant spherical particles in two dimensional shear flows. *J. Fluid Mech.* **272**, 285–318.

Hu, H. H. 1996 Direct simulation of flows of solid-liquid mixture. *Intl J. Multiphase Flow* **22**, 335–352.

Hu, H. H., Joseph, D. D. & Crochet, M. 1992 Direct simulation of fluid particle motions. *J. Theoret. Comput. Fluid Dynamics* **3**, 285–306.

Huang, P. Y., Feng, J., Hu, H. H. & Joseph, D. D. 1997 Direct simulation of the motion of solid particles in Couette and Poiseuille flows of viscoelastic fluids. *J. Fluid Mech.* **343**, 73–94.

Huang, P. Y. & Joseph, D. D. 2000 Effect of shear thinning on migration of neutrally buoyant particles in pressure driven flow of Newtonian and viscoelastic fluids. *J. Non-Newtonian Fluid Mech.* **90**, 159–185.

Jeffrey, R. C. 1964 PhD Dissertation, University of Cambridge.

Jeffrey, R. C. & Pearson, J. R. 1965 Particle motion in laminar vertical tube flow. *J. Fluid Mech.* **22**, 721–735.

Jeong, J. & Hussain, F. 1995 On the identification of a vortex. *J. Fluid Mech.* **285**, 69–94.

Johnson, A. A. & Tezduyar, T. E. 1996 Simulation of multiple spheres falling in a liquid-filled tube. *Comput. Meth. Appl. Mech. Engng* **134**, 351–373.

Johnson, A. A. & Tezduyar, T. E. 1997 3D simulation of fluid-particle interactions with the number of particles reaching 100. *Comput. Meth. Appl. Mech. Engng* **145**, 301–321.

Johnson, T. A. & Patel, V. C. 1999 Flow past a sphere up to a Reynolds number of 300. *J. Fluid Mech.* **378**, 19–70.

Joseph, D. D. 2003 *Interogations of Direct Numerical Simulation of Solid-liquid Flow*. Available on http://efluids.com/efluids/books/joseph.htm.

Joseph, D. D. & Ocando, D. 2002 Slip velocity and lift. *J. Fluid Mech.* **454**, 263–286.

Karnis, A., Goldsmith, H. L. & Mason, S. G. 1966 The flow of suspensions through tubes V. Inertial effects. *Can. J. Chem. Engng* **44**, 181–193.

Kurose, R. & Komori, S. 1999 Drag and lift forces on a rotating sphere in a linear shear flow. *J. Fluid Mech.* **384**, 183–206.

Leal, L. G. 1980 Particle motion in a viscous fluid. *Annu. Rev. Fluid Mech.* **12**, 435–476.

Magarvey, R. H. & Bishop, R. L. 1961 Transition ranges for three-dimensional wakes. *Can. J. Phys.* **39**, 1418–1422.

McLaughlin, J. B. 1991 Inertial migration of a small sphere in linear shear flows. *J. Fluid Mech.* **224**, 261–274.

McLaughlin, J. B. 1993 The lift on a small sphere in wall-bounded linear shear flows. *J. Fluid Mech.* **246**, 249–265.

Mei, R. 1992 An approximate expression for the shear lift force on a spherical particle at finite Reynolds number. *Intl J. Multiphase Flow* **18**, 145–147.

Natarajan, R. & Acrivos, A. 1993 The instability of the steady flow past spheres and disks. *J. Fluid Mech.* **254**, 323–344.

Nguyen, N. Q. & Ladd, A. J. C. 2002 Lubrication corrections for lattice-Boltzmann simulations of particle suspensions. *Phys. Rev.* E **66**, 046708.

Nott, P. R. & Brady, J. F. 1994 Pressure-driven flow of suspensions: simulation and theory. *J. Fluid Mech.* **275**, 157–199.

Oliver, D. R. 1962 Influence of particle rotation on radial migration in the Poiseuille flow of suspensions. *Nature* **194**, 1269–1271.

Pan, T.-W. 1999 Numerical simulation of the motion of a ball falling in an incompressible viscous fluid. *C. R. Acad. Sci. Paris* IIb **327**, 1035–1038.

Pan, T.-W. & Glowinski, R. 2002 Direct simulation of the motion of neutrally buoyant circular cylinders in plane Poiseuille flow. *J. Comput. Phys.* **181**, 260–279.

Pan, T.-W., Joseph, D. D., Bai, R., Glowinski, R. & Sarin, V. 2002 Fluidization of 1204 spheres: simulation and experiment. *J. Fluid Mech.* **451**, 169–191.

Pan, T.-W., Joseph, D. D. & Glowinski, R. 2001 Modeling Rayleigh-Taylor instability of a sedimenting suspension of several thousand circular particles in direct numerical simulation. *J. Fluid Mech.* **434**, 23–37.

Patankar, N. A., Huang, P. Y., Ko, T. & Joseph, D. D. 2001*a* Lift-of of a single particle in Newtonian and viscoelastic fluids by direct numerical simulation. *J. Fluid Mech.* **438**, 67–100.

Patankar, N. A., Ko, T., Choi, H. G. & Joseph, D. D. 2001*b* A correlation for the lift-of of many particles in plane Poiseuille of Newtonian fluids. *J. Fluid Mech.* **445**, 55–76.

Patankar, N. A., Singh, P., Joseph, D. D., Glowinski, R. & Pan, T.-W. 2000 A new formulation of the distributed Lagrange multiplier/fictitious domain method for particulate flows. *Intl J. multiphase flow* **26**, 1509–1524.

Phan-Thien, N., Tran-Cong, T. & Graham, A. L. 1991 Shear flow of periodic arrays of particle clusters: a boundary- element method. *J. Fluid Mech.* **228**, 275–293.

Ploumhans, P., Winckelmans, G. S., Salmon, J. K., Leonard, A. & Warren, M. S. 2002 Vortex methods for direct numerical simulation of three-dimensional bluff body flows: Application to the sphere at $Re = 300$, 500, and 1000. *J. Comput. Phys.* **178**, 427–463.

Rubinow, S. I. & Keller, J. B. 1961 The transverse force on a spinning sphere moving in a viscous fluid. *J. Fluid Mech.* **11**, 447–459.

Saffman, P. G. 1965 The lift on a small sphere in a slow shear flow. *J. Fluid Mech.* **22**, 385–400.

Sakamoto, H. & Haniu, H. 1990 A study on vortex shedding from spheres in a uniform flow. *Trans. ASME: J. Fluids Engng* **112**, 386–392.

Sakamoto, H. & Haniu, H. 1995 The formation mechanism and shedding frequency of vortices from a sphere in uniform shear flow. *J. Fluid Mech.* **287**, 151–171.

Schonberg, J. A. & Hinch, E. J. 1989 Inertial migration of a sphere in Poiseuille flow. *J. Fluid Mech.* **203**, 517–524.

Segré, G. & Silberberg, A. 1961 Radial Poiseuille flow of suspensions. *Nature* **189**, 209.

Segré, G. & Silberberg, A. 1962 Behavior of macroscopic rigid spheres in Poiseuille flow. Part 1. *J. Fluid Mech.* **14**, 115–136.

Singh, P., Hesla, T. & Joseph, D. D. 2003 Distributed Lagrange multiplier method for particulate flow with collisions. *Intl J. Multiphase Flow* **29**, 495–509.

Taneda, S. 1956 Experimental investigation of the wake behind a sphere at low Reynolds numbers. *J. Phys. Soc. Japan* **11**, 1104–1108.

Tomboulides, A. G. 1993 Direct and large-eddy simulation of wake flows: flow past a sphere. PhD Thesis, Princeton University.

Tomboulides, A. G. & Orszag, S. A. 2000 Numerical investigation of transitional and weak turbulent flow past a sphere. *J. Fluid Mech.* **416**, 45–74.

Vasseur, P. & Cox, R. G. 1976 The lateral migration of a spherical particle in two-dimensional shear flows. *J. Fluid Mech.* **78**, 385–413.

Vasseur, P. & Cox, R. G. 1977 The lateral migration of spherical particles sedimenting in a stagnant bounded fluid. *J. Fluid Mech.* **80**, 561–591.

Yu, Z., Phan-Thien, N., Fan, Y. & Tanner, R. I. 2002*a* Viscoelastic mobility problem of a system of particles. *J. Non-Newtonian Fluid Mech.* **104**, 87–124.

Yu, Z., Tanner, R. I. & Phan-Thien, N. 2002*b* Direct numerical simulation of particle migration in the Couette flow. *Proc. 6th European Conf. on Rheology, Erlangen, Germany* (ed. Münstedt, J. Kaschta & A. Merten). Institute of Polymer Materials, Friedrich-Alexander-University, Erlangen-Nürnberg, Germany.

Zhou, J., Adrian, R. J., Balachandar, S. & Kendall, T. M. 1999 Mechanisms for generating coherent packets of hairpin vortices in channel flow. *J. Fluid Mech.* **387**, 353–396.